Journal of Ocean Engineering and Science 11 (2026) 326–343

Contents lists available at ScienceDirect

Journal of Ocean Engineering and Science

journal homepage: www.elsevier.com/locate/joes

Research Paper

Multi-layered heat source model for fiber laser welding of cryogenic steel

Changmin Pyo [a,b], Jaewoong Kim [a,*], Hyunseok Oh [b,*]

[a] Korea Institute of Industrial Technology, Gwangju 61012, Republic of Korea
[b] Department of Mechanical and Robotics Engineering, Gwangju Institute of Science and Technology, Gwangju 61005, Republic of Korea

ARTICLE INFO

Keywords:
Fiber laser welding
Finite element analysis
Multi-layered model
Model calibration
Inverse problem

ABSTRACT

Simulation models can be effectively used to predict welding distortion and residual stress in laser welding systems. To this end, developing a sophisticated heat source model for finite element analysis (FEA) is crucial. This study proposes a novel multi-layered heat source model for FEA to predict the melting zone of the welds in fiber laser welding. The proposed model has multiple degrees of freedom sufficient to simulate various heat sources. A systematic approach by solving inverse problems with global optimization is devised to estimate heat source model parameters. To achieve this, a simplified FEA model is incorporated to accelerate the simulation process. Experimental results using 9% nickel steel indicate that the proposed framework provides more accurate predictions on the melting zone of the welds than existing methods while reducing the computational cost by 1/2000. The proposed framework can be used by field engineers to find the relevant heat source subjected to on-site welding conditions, minimizing trials and errors. With this method, fast and accurate welding simulations can be performed, ultimately leading to improved productivity.

1. Introduction

Regulations on fossil fuel usage have become stringent, impacting ships engaged in global goods transportation. Specifically, regulatory measures on diesel engine emissions, particularly sulfur and nitrogen oxides, are being progressively tightened, prompting a shift towards the use of natural gas as fuel [1–3]. To this end, the maritime industry put a lot of research effort into developing liquefied natural gas (LNG) fuel storage containers. Various types of fuel tanks are employed, and related studies are conducted [4,5]. LNG is known for its efficiency as its volume reduces significantly when liquefied compared to its gaseous state. However, the adoption of LNG presents challenges due to its low boiling point of -163°C. Under such conditions, most metals exhibit brittleness, necessitating careful selection and design of materials for LNG storage. The International Maritime Organization has specified suitable materials for LNG storage through the International Gas Carrier Code, including 304L stainless steel, 316L stainless steel, invar (36% nickel steel), high manganese steel, and 9% nickel steel [6].

9% nickel steel stands out for its excellent mechanical properties under cryogenic conditions, making it the primary material for LNG storage [7,8]. Yun et al. [7] conducted a study to determine the optimal welding method for fillet welding on 9% nickel steel. Kim et al. [8] investigated the fundamental design of an LNG-fueled ship using 9% nickel steel. They evaluated the performance of welded components after flux-cored arc welding (FCAW), based on design-derived thickness. However, manual welding methods like FCAW are susceptible to the arc bias phenomenon in 9% nickel steel due to magnetization, resulting in welding defects such as convex welding beads or even welding inability [9–11].

Automatic welding methods using lasers have gained popularity to address the limitations of manual welding. Arc welding is vulnerable to decreased welding strength and fractures due to structural changes in the melting area from prolonged heat exposure and significant thermal plastic distortion caused by a widely distributed heat-affected zone [13]. Laser welding, known for its speed and reliability [12], is increasingly appealing to the shipbuilding industry, which commonly relies on arc welding. In particular, fiber laser welding can mitigate the disadvantages by delivering a high heat input in a short time, minimizing structural changes in the molten zone, and reducing the heat-affected zone's area, thereby reducing thermoplastic distortion [14].

Various laser welding methods have been developed, including Nd:YAG and CO_2 laser welding [15,16]. Fiber welding using optical fiber has gained prominence due to superior beam quality and high welding power. The use of optical fibers enables precise delivery of laser pulses. The pulse dynamics governing their interaction with materials made it possible to investigate energy penetration depth [17–20]. Fluid

* Corresponding authors.
E-mail addresses: kjw0607@kitech.re.kr (J. Kim), hsoh@gist.ac.kr (H. Oh).

https://doi.org/10.1016/j.joes.2025.08.003
Received 31 May 2023; Received in revised form 20 July 2025; Accepted 8 August 2025
Available online 8 August 2025

dynamics approaches were employed to study the formation and evolution of keyholes, a prominent feature of laser welding [21,22]. Additionally, numerous simulations were conducted to reflect phase changes during the welding process [23,24].

Prediction of welding-induced distortion and residual stress is important in the shipbuilding and offshore industries, where welding is extensively applied. FEA has been commonly used to ensure the structural stability of welded structures under design loads and to establish appropriate designs [25–30]. For example, Azari-Dodaran and Ahmadi [25] assessed the stability of welded pipe structures under axial loading at elevated temperatures induced by fire, while Rathinam et al. [26] and Pranesh et al. [27] evaluated the structural performance of welded cylindrical shells and spherical pressure hulls under external pressure using FEA. However, these studies did not consider the effects of welding-induced distortion and residual stress, which can undermine the consistency of simulation outcomes. Zhou et al. [28] investigated the cryogenic fatigue and fracture toughness of welded specimens made of 5% nickel steel through a combination of experiments and simulations. Fatigue properties were predicted based on the stress distributions obtained from FEA. However, welding-induced initial distortion and residual stress were not considered in the simulations, posing limitations in terms of fidelity. Incorporating these factors into the analysis is expected to improve the reliability of structural evaluations for welded components. Yi et al. [29] conducted a simulation using a continuous heat source to predict welding distortion in a propeller base structure. However, specific details regarding the derivation, dimensions, and shape of the heat source were not provided, making it difficult to generalize the model to other welding conditions. Saini et al. [30] evaluated the structural integrity of welded pipe structures during offshore installation by accounting for residual stresses through a hot spot stress approach, which incorporated weld joint dimensions and geometry to apply appropriate stress concentration factors. While this method improves fatigue life prediction at critical locations such as weld toes, it does not consider initial welding distortion, limiting its comprehensiveness [31]. To improve simulation fidelity, sophisticated and generalizable welding heat source models are required. These models allow reliable prediction of both initial distortion and residual stress across the entire weld joint.

Several heat source models were proposed to predict weld distortion under particular conditions of fiber laser welding. Nonetheless, existing heat source models are not flexible enough to predict the shape of the weld zone boundary since the model form has limited degrees of freedom (DOF). Moreover, it is challenging to estimate model parameters due to the dearth of systematic approaches to determine model parameters. To address the challenges, this study proposed a novel multi-layered heat source model for fiber laser welding. A systematic approach by solving inverse problems was proposed to determine an optimal set of the model parameters.

The remaining sections of this paper are organized as follows. Section 2 presents a literature review. Section 3 describes the proposed framework, including experiments, heat source modeling, model parameter selection, and FEA simulations. Section 4 shows the results and discussions. Finally, conclusions and future work are followed in Section 5.

2. Literature review and modeling approach

Simulations using FEA have been instrumental in predicting fiber laser welding distortion, leading to the proposal of various heat source shapes [32–45]. Unlike arc welding, which commonly relies on Goldak's double elliptic heat source model [46], laser welding lacks a dominant representative heat source model. This absence challenges field engineers in selecting an appropriate model for their specific applications.

Various types of shape models have been proposed to model heat sources for laser welding. The shapes and characteristics of these models are summarized in Table 1 and depicted in Fig. 1. The circular cone shape model was proposed by Kim et al. [32]. Truncated cone models and variants were also developed [33–37]. For example, Xu et al. [36] proposed a truncated cone model where the bevel was a second-order polynomial curve. Evdokimov et al. [37] proposed a model where the bevel was an exponential curve. In the aforementioned models, the size of a heat source decreases as it progresses from the laser irradiation surface to the inside of a base material. Other models were also studied, where the size of a heat source decreases along the depth of a base material and then increases again. For instance, a combination of two truncated cones and a combination of a truncated cone and a cylinder were developed [38–41]. Specifically, Unni and Vasudevan [41] proposed various types of combination models, such as the rotary Gaussian model. The models were validated under particular conditions, and meaningful results were obtained for predicting thermoplastic distortion. Giudice et al. proposed a heat source model for laser beam welding based on a multipoint-line analytical model [42] and conducted multi-physics numerical simulations [43]. Additionally, residual stress was evaluated using the methods [44]. Laser welding has continuously

Table 1
Types of heat source models.

	Shape of heat source	Ref. No.
1	Cone model	[32]
2	Truncated conical model, Combination model (Conical with cylindrical shell, Conical with conical shell)	[33–35]
3	Truncated conical model with 2nd order polynomial curve	[36]
4	Truncated conical model with an exponential curve	[37]
5	Combination model (Conical with cylindrical shell)	[38]
6	Truncated conical model, Combination model (Conical with double ellipsoidal model, Conical with cylindrical shell)	[39]
7	Combination model (Double truncated model)	[40]
8	Truncated conical model Goldak double-ellipsoidal model Volumetric Gaussian model Rotary Gaussian model Combination model (Conical with cylindrical shell)	[41]
9	Parameterized multipoint-line analytical model	[42–44]
10	Double ellipsoidal model (Arc welding)	[46]
11	Avocado shape model (High speed arc welding)	[47]
12	Representative laser heat source models (Levels 1 and 2)	[48,49]

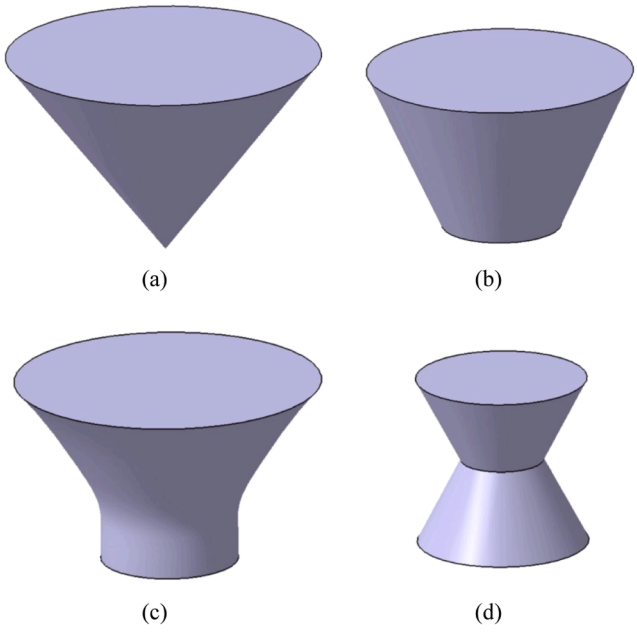

Fig. 1. Shapes of the diverse heat source models (a) Cone model, (b) Truncated conical model, (c) Truncated conical model with curve, and (d) Combination model (conical with conical shell).

introduced various heat source models, each of which effectively describes the phenomena under specific conditions [45].

Various heat source models paradoxically highlight the absence of a representative heat source for laser welding. This diversity challenges field engineers to select an appropriate model for specific operational conditions. Moreover, identifying relevant parameters within heat source models is complex due to varying welding conditions in real-world applications, hindering practical implementation.

This study aims to assist on-site engineers in deriving heat source models and corresponding parameters tailored to specific welding conditions. To address this issue, a composite model is proposed, comprising multiple truncated conical layers based on Gaussian distributions. The model consists of six layers and is designed to reflect the characteristics of existing heat source models. Furthermore, a framework is introduced to determine the key dimensions defining the heat source. This approach integrates optimization algorithms and FEA to develop a heat source model adapted to field conditions, facilitating seamless application in practical welding scenarios.

A multi-layered heat source model for laser welding was developed to provide flexibility for various welding conditions [48,49]. The model is delineated across three levels, with the level 1 model serving to validate the technical viability of the multi-layered heat source model. As depicted in Table 2 and Fig. 2, the level 1 model comprises five layers and maintains 11 variables in an unknown state, subsequently determining the variables using a global optimization algorithm. With this model, welding heat source models were developed for two specific welding conditions, confirming their technical feasibility as representative heat source models [48]. However, the level 1 model did not account for correlations between variables. As a result, it was found that heat source models with irregular shapes were fundamentally different from those identified in previous studies.

The level 2 heat source model was proposed to address this limitation, which reduced the number of independent variables by establishing a relationship between the heat energy ratio and radius for each layer [49]. In the study, a relationship was derived between the shape and heat energy ratio of individual heat source layers.

This derivation assumes that the thermal energy at the center of a heat source remains constant regardless of its depth, which is consistent with previously proposed heat source models. The correlation was reflected between the sizes of layer volumes and the heat energy ratio of each layer. Additionally, the upper shape of the heat source exhibited a conical form, a common feature of conventional heat source models, wherein the laser irradiation surface has a larger radius than the inner surface of the base material. Given this consideration, a relationship between the radii forming the upper layer was established. The primary independent variables of the heat source level 2 model are outlined in Table 3. The level 2 model minimized the number of independent variables by analyzing and defining the search space of key relationships, effectively addressing the irregular shape issues encountered in the level 1 model.

Table 2
Principal parameters of the heat source level 1 model [48].

Variables	Definition
η	Welding power efficiency
R_{T1}	Top radius of the 1st layer (top layer)
R_{T2}	Top radius of the 2nd layer
R_{T3}	Top radius of the 3rd layer
R_{T4}	Top radius of the 4th layer
R_{T5}	Top radius of the 5th layer
R_B (=R_{T6})	Bottom radius of the 5th layer
H_{r1}	Heat ratio of the 1st layer
H_{r2}	Heat ratio of the 2nd layer
H_{r3}	Heat ratio of the 3rd layer
H_{r4}	Heat ratio of the 4th layer
H_{r5}	Heat ratio of the 5th layer
Heat depth ($y_{T1} - y_{T6}$)	Length of heat source in the depth direction

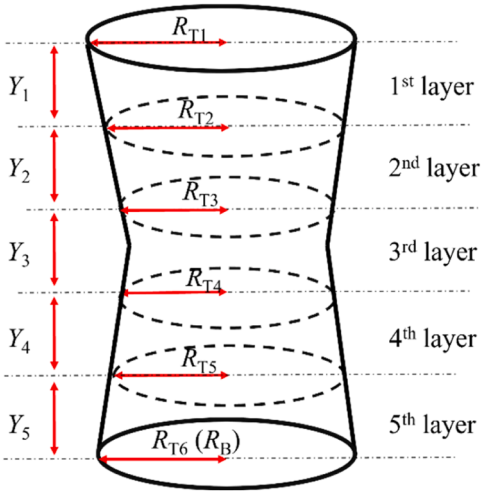

Fig. 2. Shape of the heat source for the level 1 and level 2 models.

Table 3
Principal independent variables of the level 2 heat source model [49].

Variables	Definition
η	Welding power efficiency
R_{T1}	Radius of the top of the 1st layer (top layer)
R_{T4}	Radius of the top of the 4th layer
R_{T5}	Radius of the top of the 5th layer
R_{T6}	Radius of the bottom of the 5th layer
Heat depth ($y_{T1} - y_{T6}$)	Length of the heat source in the depth direction
C_{RT1}	Coefficient of R_{T1} and R_{T2}
C_{RT2}	Coefficient of R_{T2} and R_{T3}
W_{HR1}	Weighted rate of H_{r1}

The level 3 model of this paper addressed the issues that remained unresolved in the level 2 model. This model has been enhanced to depict the existing model fundamentally while simultaneously achieving a more precise representation of finer details. To achieve this, the previous multi-layered heat source model with an odd number of layers was modified to a model consisting of an even number of six layers. This adjustment aims to reflect that the combination model has a turning point at the center of the vertical direction of a heat source model [38–41]. Additionally, the relationship between the radii of the lower layer was defined. Unlike conventional models where the size of the radius of a lower layer consistently increases or decreases, the level 2 model encountered an inconsistency in the direction of size, resulting in awkward shapes as depicted in Fig. 3 [50]. The shape of the heat source model used in the level 3 model effectively addressed these issues, as illustrated in Fig. 4.

The two-dimensional (2D)-based simplified model was validated and employed to overcome the limitation of requiring a significant amount of computational time. This stemmed from the fact that more than 2,000 simulations are required to find an optimal set of model parameters. The efficacy of this method was verified when deriving the heat source model of arc welding [51]. Consequently, the simplified model is 2,000 times faster than the original model.

The movement of the molten pool has been investigated in several studies for laser welding. Computational fluid dynamics (CFD) has been used to analyze the flow of the molten pool generated by laser welding and to predict the keyhole geometry formed by the flow. Ciancio [52] presented a heat flow model for viscoelastic media to establish the foundation for heat transfer analysis, considering the behavior of molten pools. A CFD analysis was conducted to predict the molten pool flow behavior in the process of laser welding. Nevertheless, it falls short in offering approaches for predicting welding distortion and residual stresses essential for on-site applications. Consequently, this study

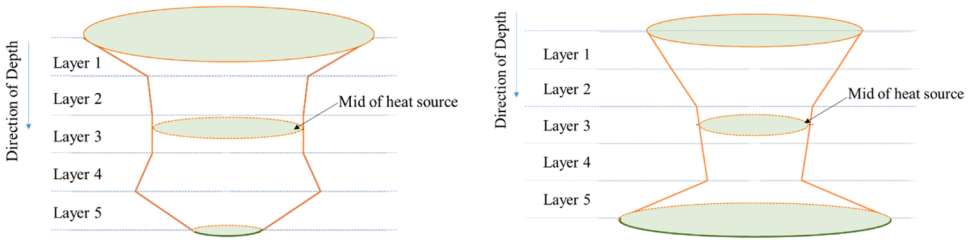

Fig. 3. The level 2 heat source model in [50] (a) Case 1 and (b) Case 2.

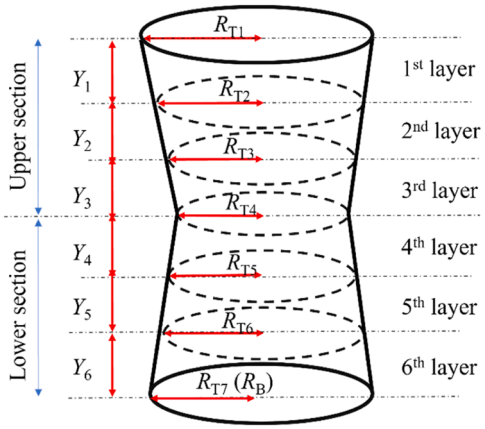

Fig. 4. The level 3 heat source model proposed in this study.

introduces a novel academic contribution by proposing an advanced heat source model, addressing this previously unexplored aspect more precisely.

3. Proposed framework

The proposed framework consists of (1) experiments, (2) heat source modeling, (3) model parameter selection, and (4) FEA simulations. This study aims to derive an appropriate heat source model for given welding conditions. First, bead-on-plate (BOP) welding experiments are conducted using a fiber laser welder, followed by observation of the cross-sectional shape and comparison with the temperature distribution of the melting zone in thermal transfer simulations. Second, a multi-layered heat source model is proposed. Third, a systematic approach is employed to estimate the model parameters by solving inverse problems. Finally, FEA simulations are conducted by adjusting model parameter values (e.g., layer radius) to obtain optimal results. The process is illustrated in Fig. 5.

Significant details related to the simulations (e.g., model dimension, mesh type, and boundary conditions) and the constraints and objective functions used in the optimization process were disclosed. Ethical considerations and potential risks associated with the research have been comprehensively addressed. Contents from other studies have been paraphrased and relevant data have been included as references.

3.1. Experiments

Bead-on-plate welding using 9% nickel steel was performed. Its chemical composition and principal mechanical properties detailed in Tables 4 and 5 [53]. A fiber laser welding machine with the welding power capacity of 5 kW was employed for the experiments. Miyachi welding equipment (Miyachi, Japan) was employed, comprising a laser welding oscillator, optical system, controller, and chiller, as shown in Fig. 6. The optical system specifications include a spot diameter of 400 μm, a focal length of 148.8 mm, a focal depth of 6 mm, and a defocus of 0. Nitrogen (N_2) was used as a protective gas at a rate of 15 L/min. Both the tilting and working angles were maintained at 0°.

The welding power was set at 4 kW. Experiments were conducted with varying speeds between 1.0 m/min and 1.5 m/min. Welded specimens measuring 60 mm × 100 mm × 6 mm were used, with cross-sectional observations performed after cutting the center part to 10 mm in the welding direction and 25 mm in the width direction. Polishing was conducted to facilitate clear observation of the bead shape, followed by etching using a Nital solution (10% HNO_3, Ethanol). A digital optical microscope with a resolution of two mega-pixels was used to measure the shape of each weld bead. The bead and penetration were subsequently observed by the cross-sectional analysis. For comparison with FEA results, welding shapes were classified based on top bead width and penetration. The primary indicators measured in the welding shape are illustrated in Fig. 7.

3.2. Proposed heat source model

The novel heat source model is proposed based on a multi-layered configuration to perform heat transfer simulations that emulate the laser welding process. The proposed model serves as a representative heat source model capable of encompassing the majority of existing models. As detailed in the literature review section, this model represents a level 3 enhancement, addressing limitations identified in the levels 1 and 2 models.

The level 3 model was designed to incorporate shapes from previous models while excluding awkward configurations. Two primary enhancements were implemented. First, the number of layers was increased to an even number (from five to six) to emulate combination models better. Second, a relationship between the radii of the lower layer was introduced to eliminate irregular shapes. These improvements characterize the level 3 model.

The heat source distribution within each layer followed a Gaussian distribution in the level 3 heat source model. The heights of all layers remained consistent. Eqs. (1)–(5) below depict the heat source distribution for each layer, with the meanings of the variables provided in Table 6. Eq. (1) represents the total energy distribution of the heat source, indicating that it consists of the sum of the energy distribution of each layer. Eq. (2) describes the energy distribution in each layer, following a Gaussian distribution based on the energy distribution formula for a truncated conical shape. Eq. (3) represents the maximum energy value for each layer. Eq. (4) is used to derive the value of $R_n(y)$, where $R_n(y)$ represents the radius that varies depending on the depth direction in the truncated conical shape. Eqs. (2) and (3) are referenced from a prior study on the energy distribution equation for a truncated conical shape [33]. Lastly, Eq. (5) represents the total amount of welding heat energy reflecting welding efficiency, calculated as the product of welding efficiency, voltage, and current.

$$q(x,y,z) = \sum_{n=1}^{6} H_n \times q_n(x,y,z), \tag{1}$$

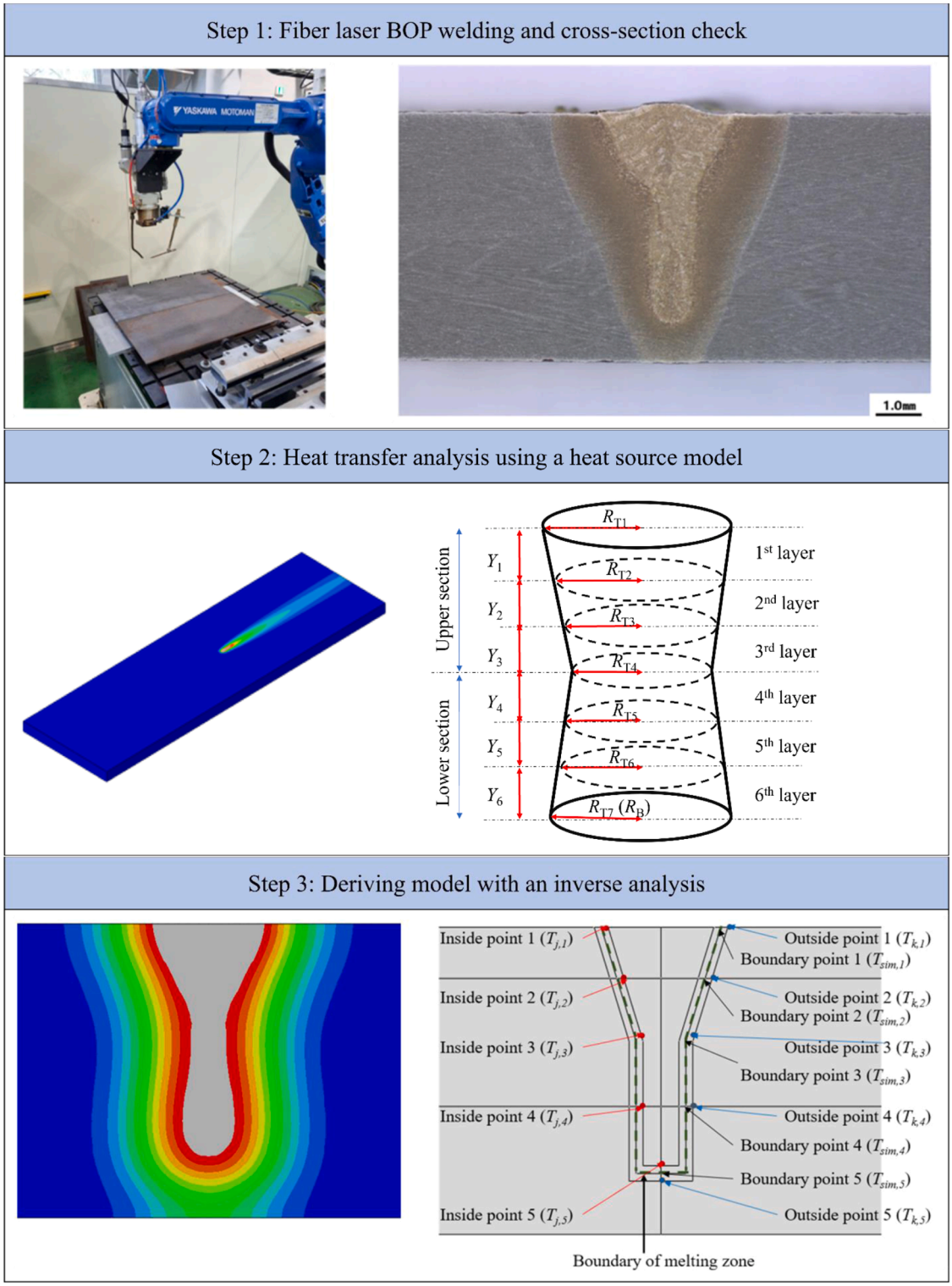

Fig. 5. Process for the derivation of the heat source model.

Table 4
Chemical composition of 9% nickel steel (wt.%).

Component	C	Si	Mn	S	P	Ni	Fe
Percentage (wt.%)	0.050	0.670	0.004	0.003	0.250	9.020	Bal.

Table 5
Mechanical properties of 9% nickel steel.

Yield strength (MPa)	Tensile strength (MPa)	Elongation (%)	Hardness (HV)
651.6	701.1	26.6	243.0

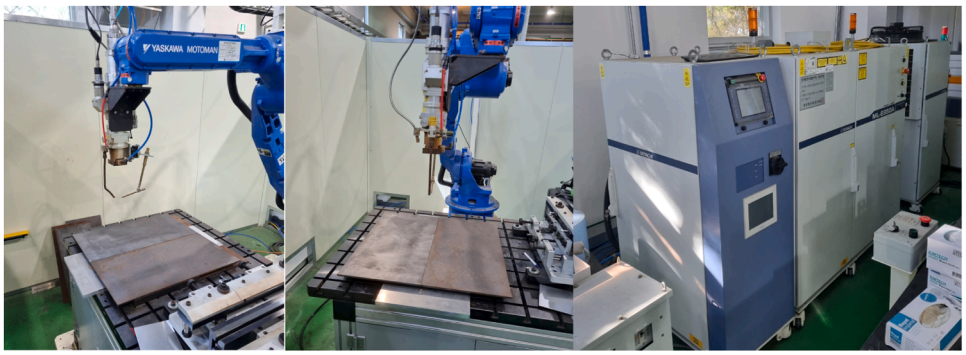

(a) (b) (c)

Fig. 6. Fiber laser welding system: (a) Side view of the welding machine, (b) Front view of the welding machine, and (c) Laser control system.

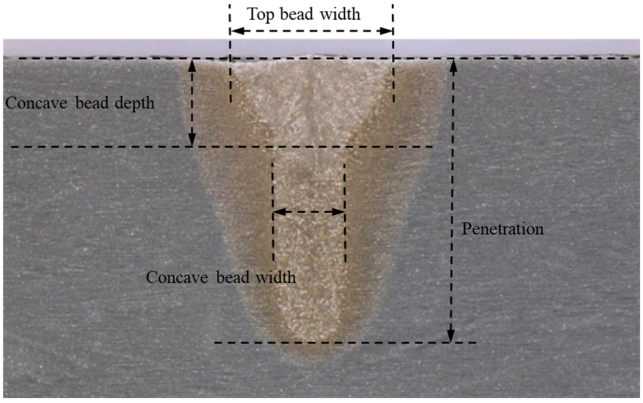

Fig. 7. Cross-sectional view after laser welding.

Table 6
Variables and definitions.

Variable	Definition
Q	Power of the laser source with the welding efficiency
V	Voltage of the laser source
I	Current of the laser source
η	Welding power efficiency
R_{Tn}	Radius of the top of the n^{th} layer (top layer)
H_n	Heat ratio of the n^{th} layer
$q(x,y,z)$	Total energy distribution
$q_n(x,y,z)$	Energy distribution of the n^{th} layer
q_m	Maximum energy of each layer
x	Direction of the welding
y	Direction of the depth
z	Orthogonal direction of x and y
$R_n(y)$	Radius of the n^{th} layer along y
y_{Tn}	Depth to top of the n^{th} layer
δ	Thickness of each layer

$$q_n(x,y,z) = q_m \times \exp\left[-\frac{3\{(x-vt)^2+z^2\}}{R_n(y)^2}\right], \tag{2}$$

$$q_m = \frac{9Qe^3}{\pi\delta(e^3-1)\left(R_{Tn}^2+R_{Tn}R_{Tn+1}+R_{Tn+1}^2\right)}, \tag{3}$$

$$R_n(y) = R_{Tn} - (R_{Tn}-R_{Tn+1}) \times \frac{y_{Tn}-y}{y_{Tn}-y_{Tn+1}}, \tag{4}$$

$$Q = \eta V \times I. \tag{5}$$

It was observed that the inflection of a heat source occurred at most once when reviewing previous models, as illustrated in Fig. 8. Additionally, it should be noted that the inflection occurred at the center part in the height direction. By defining the center as an inflection point, this model can simulate cases where an inflection occurs or does not occur.

The radius equation of a layer constituting the lower heat source is shown in Eqs. (6)–(9). These equations account for two types of shapes, each capable of reflecting either scenario. In one situation, similar to the upper heat source, the radius of a lower heat source continuously decreases as it progresses in the depth direction. In the other scenario, unlike the upper heat source, the radius of the lower heat source continuously increases in the depth direction.

$$R_{T5} = 0.0001 + (R_{T4} - 0.0001) \times C_{RT4}, (0 \le C_{RT4} \le 1.5) \tag{6}$$

$$R_{T6} = 0.0001 + (R_{T5} - 0.0001) \times (C_{RT5} + D/2), (0.5 \le C_{RT5} \le 1.0) \tag{7}$$

$$R_{T7} = 0.0001 + (R_{T6} - 0.0001) \times (C_{RT6} + D/2), (0.5 \le C_{RT6} \le 1.0) \tag{8}$$

$$D = 0.5 \times ((C_{RT4} - 1)/\mathrm{abs}(C_{RT4} - 1)) + 0.5. \tag{9}$$

R_{T4} represents the radius of the center in the height direction, while R_{T5}, R_{T6}, and R_{T7} denote the bottom radius of layers 4, 5, and 6, respectively. C_{RT4} is the parameter between R_{T4} and R_{T5}. Eqs. (6)–(8) depict the relationships between the radii of the layers in the lower region of the heat source, with each layer based on a truncated conical shape where the inclined plane is a first-order curve. This contrasts with the level 2 model, which permits the radius of the heat source to increase or decrease in the lower region. Eq. (9) represents the determinant value, shaping the heat source. Additionally, by configuring three layers at the bottom, the model is designed to simulate truncated conical shapes where the inclined plane is not only a straight line but also a quadratic or exponential curve.

The determinant value D is determined by C_{RT4}. When C_{RT4} is less than one, D is equal to zero; when C_{RT4} is greater than one, D is equal to one. When D is zero, R_{T6} and R_{T7} become smaller than R_{T5} and R_{T6}, respectively. This indicates that the radius of the lower heat source decreases along the depth direction. On the other hand, when D is one, the radius increases with depth, as described in Eqs. (7) and (8).The relationship among the radii between the layers for the upper heat source was configured to reflect previous studies. In the studies, the radius of the heat source decreases as it penetrates from the surface to the inside of the base material. The radius size was set to decrease toward the center in the height direction, and the corresponding equation is as follows. Additionally, the energy ratio of each layer of a heat source is set in proportion to the volume ratio of each layer, as in the level 2 heat source model. This ensures that the amount of heat energy in the center remains consistent across layers [49].

$$R_{T2} = 0.0001 + (R_{T1} - 0.0001) \times C_{RT1}, (0 \le C_{RT1} \le 1.0) \tag{10}$$

$$R_{T3} = 0.0001 + (R_{T2} - 0.0001) \times C_{RT2}, (0 \le C_{RT2} \le 1.0) \tag{11}$$

$$R_{T4} = 0.0001 + (R_{T3} - 0.0001) \times C_{RT3}.(0 \le C_{RT3} \le 1.0) \tag{12}$$

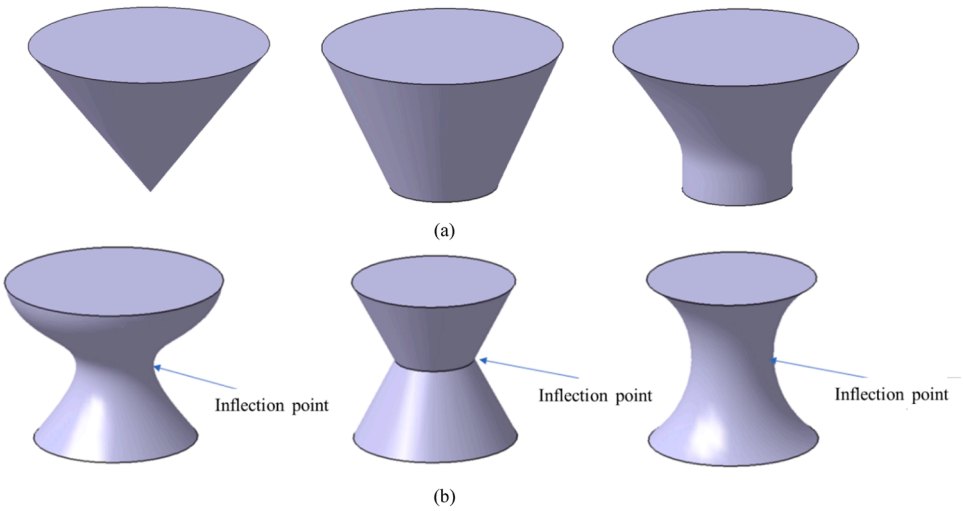

Fig. 8. Number inflections of existing heat source models (a) Models without inflection and (b) Models with one inflection.

The radius in the upper region of the heat source decreases from the top to the center in the depth direction. This is represented by Eqs. (10)–(12). Additionally, the model is designed to simulate truncated conical shapes, where the inclined plane is not limited to a straight line. It can also take the form of a quadratic or exponential curve throughout the entire upper region, similar to the configuration in the lower region.

3.3. Model parameter selection

Ten variables were employed as independent variables to determine the shape of a multi-layered (six-layer) heat source model. The list of related variables is provided in Table 7. To execute the optimization algorithm, it is crucial to establish the range of these variables. The range of variables was defined extensively to achieve accurate results, as depicted in Table 8. The range of C_{RT4}, C_{RT5}, and C_{RT6}, which dictates the shape of the lower region, is determined in accordance with the information described in Section 3.2. For reference, the independent variables used in levels 1 and 2 are presented in Tables 9 and 10, respectively; these values were updated to accommodate the use of six layers instead of five layers. Model calibration is essential to determining a set of optimal model parameters. In this study, an optimization-based model calibration method was used. The objective is to identify model parameters that maximize the agreement between the FEA and experimental results. Eq. (13) defines the temperature disagreement between the FEA simulation and experimental results (L).

$$L = \sum_{i=1}^{n} \left| T_{\exp,i} - T_{\mathrm{sim},i}^{\max} \right|. \tag{13}$$

$T_{\exp,i}$ is the melting point of the cryogenic steel at the i^{th} location of the melting zone boundary from experiments; $T_{\mathrm{sim},i}^{\max}$ is the maximum temperature value at the i^{th} location during the welding process; n is the total number of inspection locations used to evaluate the temperature disagreement between the FEA simulations and experimental results; It was assumed that the temperature distribution at the melting zone boundary (i.e., $T_{\exp,i}$) is the melting point of the cryogenic steel (i.e., 1450°C) since the welding zone denotes the area where the temperature is at the melting point during welding. L is used as the objective function during the optimization process. Constraints were also established based on temperature considerations. Specifically, the temperature of the outside checkpoint should not surpass the melting point during the welding process. Conversely, the temperature of the inside checkpoint should exceed the melting point, even if only for a brief period, during

Table 7
Variable values of the level 3 heat source model.

Variables	Definition
η	Welding power efficiency
R_{T1}	Radius of the top of the 1st layer (top layer)
Heat depth $(y_{T1} - y_{T7})$	Length of the heat source in the depth direction
C_{RT1}	Coefficient of R_{T1} and R_{T2}
C_{RT2}	Coefficient of R_{T2} and R_{T3}
C_{RT3}	Coefficient of R_{T3} and R_{T4}
C_{RT4}	Coefficient of R_{T4} and R_{T5}
C_{RT5}	Coefficient of R_{T5} and R_{T6}
C_{RT6}	Coefficient of R_{T6} and R_{T7}
W_{HR1}	Weighted rate of H_1

Table 8
Range of variables of the optimization algorithm.

Variables	Min.	Max.
η	79.8	92.4
R_{T1}	0.1	10.0
Heat depth $(y_{T1} - y_{T7})$	0.1	10.0
C_{RT1}	0.0	1.0
C_{RT2}	0.0	1.0
C_{RT3}	0.0	1.0
C_{RT4}	0.0	1.5
C_{RT5}	0.5	1.0
C_{RT6}	0.5	1.0
W_{HR1}	1.0	1.2

Table 9
Independent variables used in the level 1 model.

Variables	Definition
η	Welding power efficiency
R_{T1}	Top radius of the 1st layer (top layer)
R_{T2}	Top radius of the 2nd layer
R_{T3}	Top radius of the 3rd layer
R_{T4}	Top radius of the 4th layer
R_{T5}	Top radius of the 5th layer
R_{T6}	Top radius of the 6th layer
R_B (=R_{T7})	Bottom radius of the 6th layer
H_{r1}	Heat ratio of the 1st layer
H_{r2}	Heat ratio of the 2nd layer
H_{r3}	Heat ratio of the 3rd layer
H_{r4}	Heat ratio of the 4th layer
H_{r5}	Heat ratio of the 5th layer
H_{r6}	Heat ratio of the 6th layer
Heat depth $(y_{T1} - y_{T7})$	Length of the heat source to the depth direction

Table 10
Independent variables used in the level 2 model.

Variables	Definition
η	Welding power efficiency
R_{T1}	Radius of the top of the 1st layer (top layer)
R_{T4}	Radius of the top of the 4th layer
R_{T5}	Radius of the top of the 5th layer
R_{T6}	Radius of the top of the 6th layer
R_{T7}	Radius of the bottom of the 6th layer
Heat depth $(y_{T1} - y_{T7})$	Length of the heat source to the depth direction
C_{RT1}	Coefficient of R_{T1} and R_{T2}
C_{RT2}	Coefficient of R_{T2} and R_{T3}
C_{RT3}	Coefficient of R_{T3} and R_{T4}
W_{HR1}	Weighted rate of H_{r1}

the welding process. Outside checkpoints were located outside the borderline of the melting zone, while inside checkpoints were positioned on the inside. Both were placed at a distance of 0.2 mm from the borderline. This study employed a combination of constraints and objective functions to derive precise values, and the constraints are detailed in Eqs. (14) and (15).

$$T_m - \mathrm{Max}(T_j) < 0, \tag{14}$$

$$T_m - \mathrm{Max}(T_k) > 0. \tag{15}$$

T_i is the temperature values at the inside points; T_k is the temperature values at the outside points in Fig. 9. The algorithm employed in this study is the multi-island genetic algorithm (MIGA) model, which is a global optimization algorithm. The genetic algorithm operates as an exploratory algorithm based on the principles of survival of the fittest and inheritance mechanisms. It evaluates the fitness of each individual in the population every generation, using a population composed of numerous individuals. It selectively propagates genes that adapt well to the given environment, performs crossover, and generates new offspring. Additionally, mutations can occur in specific genes of individuals with a given probability, leading to changes in genetic traits and facilitating the exploration of unexplored areas. Through this iterative process, where superior genetic traits are reproduced in subsequent generations, genes better suited for the given environment are retained, as depicted in Table 11 [54].

MIGA introduces subgroups and periodically exchanges individuals between these subgroups to enhance optimization efficiency over a broader range [55]. The principal process of the MIGA approach is illustrated in Fig. 10. This algorithm is widely used in various industries, including electronics, for design optimization purposes [56].

Table 11
Procedures for implementing the genetic algorithm [54].

Sequence	Contents	Sequence	Contents
Step 1	A random population is created.	Step 6	Change the genes of a new population according to mutation rate.
Step 2	Evaluate fitness $f(x)$.	Step 7	Accept a new population.
Step 3	Create a new population.	Step 8	Replace with a new population.
Step 4	Select two superior populations according to the survival of the fittest principle.	Step 9	Stop when the end condition is satisfied.
Step 5	Perform crossover for the genetic sequences of two individuals according to the crossover rate to produce an offspring generation.	Step 10	Repeat Steps 2 to 9.

3.4. FEA simulations with the simplified model

The objective of this study is to develop a welding heat source model capable of simulating the cross-sectional shape resulting from bead-on-plate welding experiments. To achieve this, FEA-based heat transfer simulations were conducted, incorporating a moving heat source.

Two cases were defined: Case 1 with the parameters of 4 kW power and 1.0 m/min welding speed; and Case 2 with the parameters of 4 kW power and 1.5 m/min welding speed. The simulations were conducted, taking into account experimental conditions to model real-world scenarios accurately. However, to efficiently handle the numerous simulations required for global optimization, a simplified 2D-based model was employed as depicted in Fig. 11. This approach reduced input time while maintaining consistency with the experimental setup. The finite element was 3-node linear triangles (DC2D3). The number of elements was 6,080 and 5,862, while the DOF were 6,348 and 6,124 for Cases 1 and 2, respectively. In contrast, the original three-dimensional (3D) model uses brick-shaped 8-node linear heat transfer elements (DC3D8) with an average mesh length of 0.5 mm, compared to the simplified model. The original model has 288,000 elements and 316,691 DOF.

The vertical length of the welding model in the simulations was reduced to 20 mm, which was 33.3% lower than that of the original model. This decision was based on a section with minimal temperature change in the maximum penetration area. For instance, when the welding speed is 1.0 m/min, a temperature variation of less than 1°C was observed at a distance of 7.4 mm from the center, with a narrower variation observed at 1.5 m/min.

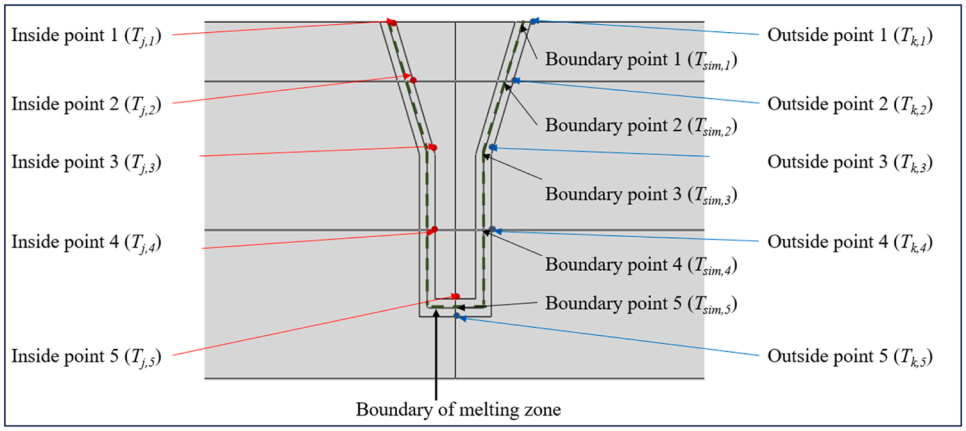

Fig. 9. Boundary of melting zone and temperature check points.

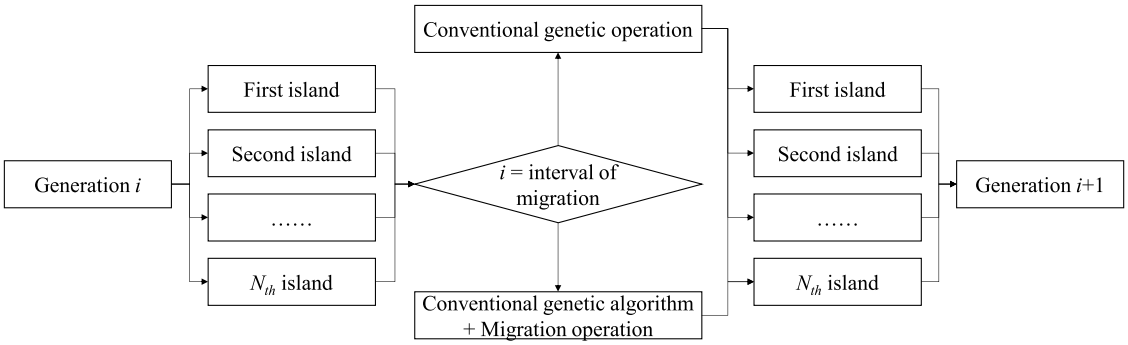

Fig. 10. Flow chart of the multi-island genetic algorithm [55].

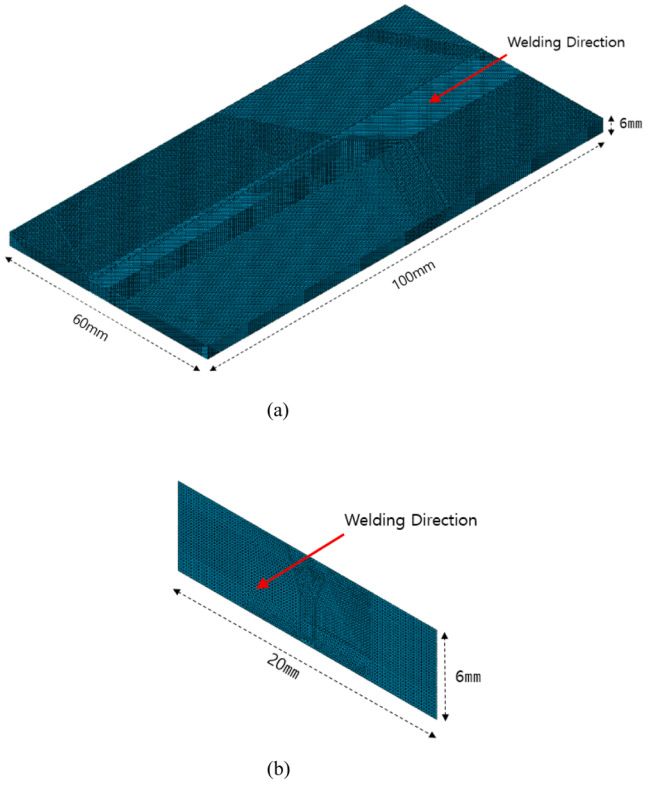

Fig. 11. Geometry of analytical modeling: (a) Original model and (b) Simplified model.

The analysis cost was reduced while minimizing the impact of boundary conditions by setting the length to 20 mm, as depicted in Fig. 12. Table 12 specifies the element type and the computational cost of each model, illustrating the effect of the simplified model. The

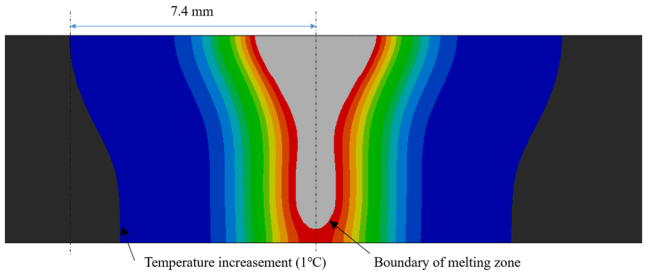

Fig. 12. Temperature change in the maximum penetration area under the condition of the welding speed of 1.0 m/min.

Table 12
The number of grids of the analysis model and time required for analysis (Case 1).

	Number of mesh (EA)	Mesh size (mm)	Mesh type	Computational cost (hours)
Original model	288,000	0.5	8-node linear heat transfer brick (DC3D8)	More than 480
Simplified model	6,080	Less than 0.2	3-node linear heat transfer triangle (DC2D3)	0.25

analysis of the consistency of the simplified model revealed a high consistency level of 10.9% compared to the original model under all conditions.

The same welding speed and power were used as in the actual experiment. Both convective and radiative heat transfer were considered for the analysis. In the thermal analysis, the boundary conditions for convection and radiation heat transfer were set as shown in Eqs. (16) and (17).

$$Q_{\text{conv}} = h_{\text{conv}} A (T - T_0) \tag{16}$$

$$Q_{\text{rad}} = \sigma \varepsilon A \left(T^4 - T_0^4\right) \tag{17}$$

Q_{conv} and Q_{rad} are the convection heat energy and the radiation heat energy, respectively; H_{conv}, σ, ε, and A are the convection heat transfer coefficient, Stefan-Boltzmann constant, emissivity of the material, and area of heat transfer, respectively. The key variables are set as follows: h_{conv} is 10 W/m^{2}K [57], ε is 0.8 [58], and T_0 is 27℃. The principal properties of the material are illustrated in Fig. 13.

The temperature distribution of the welding zone was predicted with Abaqus 2020 (Dassault Systèmes, France) by incorporating the user subroutine coded by Fortran 2021 (Intel, US) [59]. The temperature-dependent material property values were derived by JMatpro 7.0 (Sente Software, UK) [60,61]. The optimal values of the model parameters in the heat source model were obtained from Isight 2020 (Dassault Systèmes, France) [62,63]. Calculations were performed by a desktop computer with an Intel Core i9-10900 processor, DDR4-RAM of 128 gigabytes.

The temperature distribution was calculated using Fourier's law as the governing equation for heat conduction. To solve the second-order differential equation inherent in Fourier's law, a triangular mesh-based FEA was employed. Although various methods exist for handling higher-order differential equations [64,65], FEA stands out for its capability to transform such equations into algebraic matrix equations with finite elements, rendering it particularly advantageous for solving problems under nonlinear conditions. Given that this study addresses nonlinearities stemming from temperature-dependent material properties, FEA was selected as the computational approach.

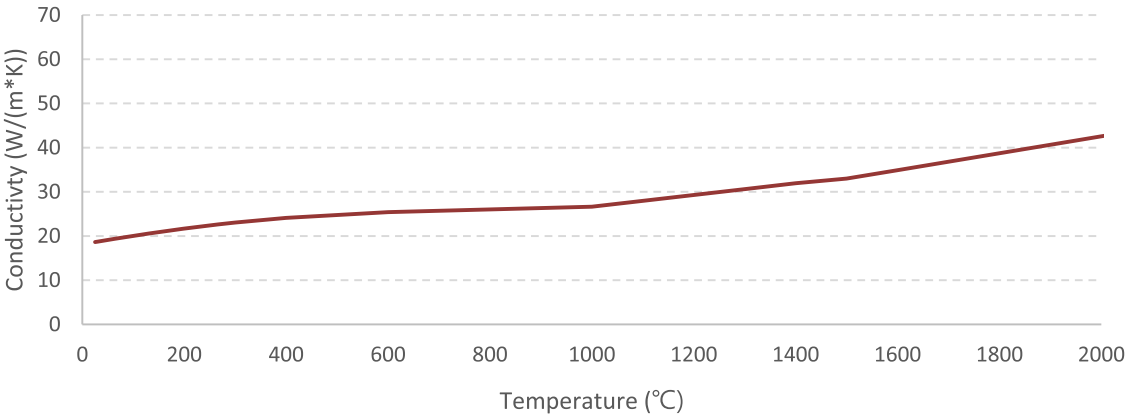

(a)

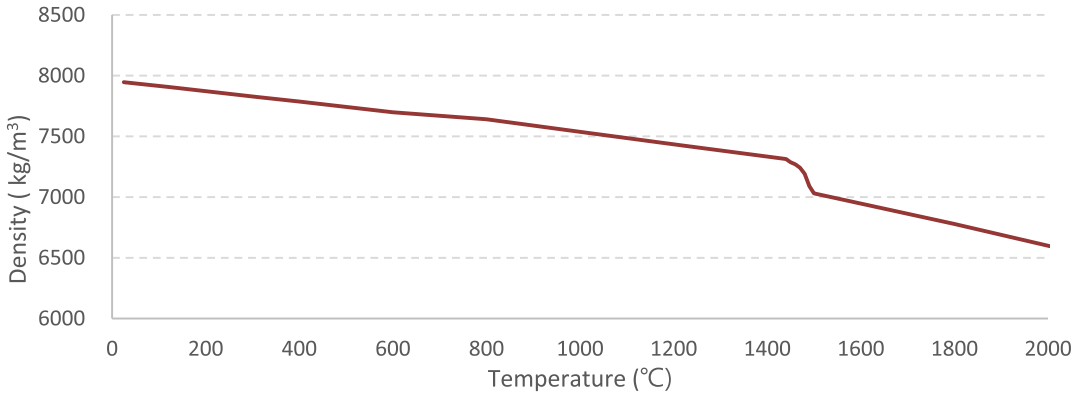

(b)

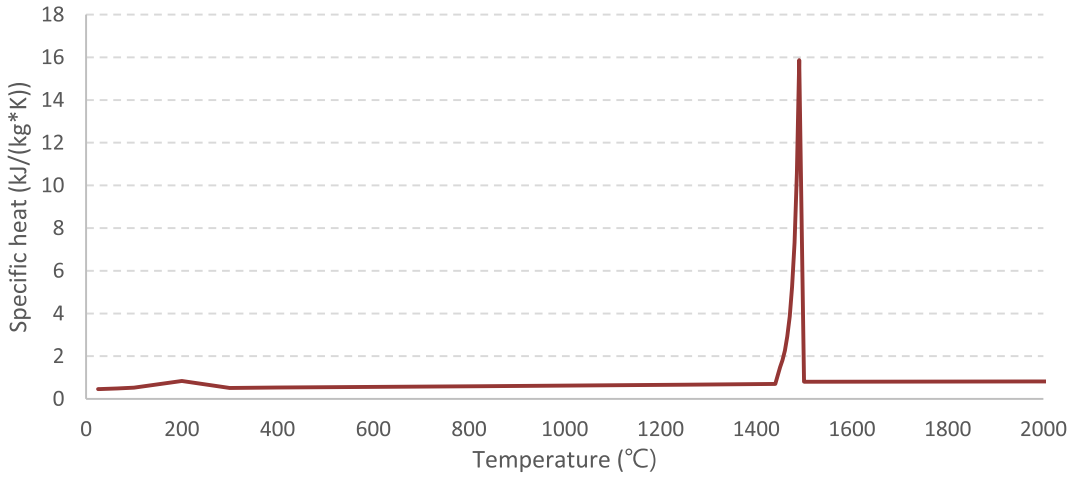

(c)

Fig. 13. Material properties of 9% nickel steel by temperature (a) Conductivity, (b) Density, and (c) Specific heat [48].

4. Results and discussions

This section is dedicated to deriving model parameter values for constructing a welding heat source model in two cases, using the findings outlined in Section 3. Simulation results are presented to validate the accuracy of the simplified FEA models. Finally, the accuracy of the FEA simulations is compared with that of the experiments.

4.1. Heat source models

The multi-layered (six-layer) heat source model was derived through the process described in Section 3 under two-speed conditions (1.0 and 1.5 m/min), using 9% nickel steel under the condition of 4 kW welding power. The temperature distribution over time is depicted in Fig. 14. The size of the welding bead, which is the result of cross-section analysis

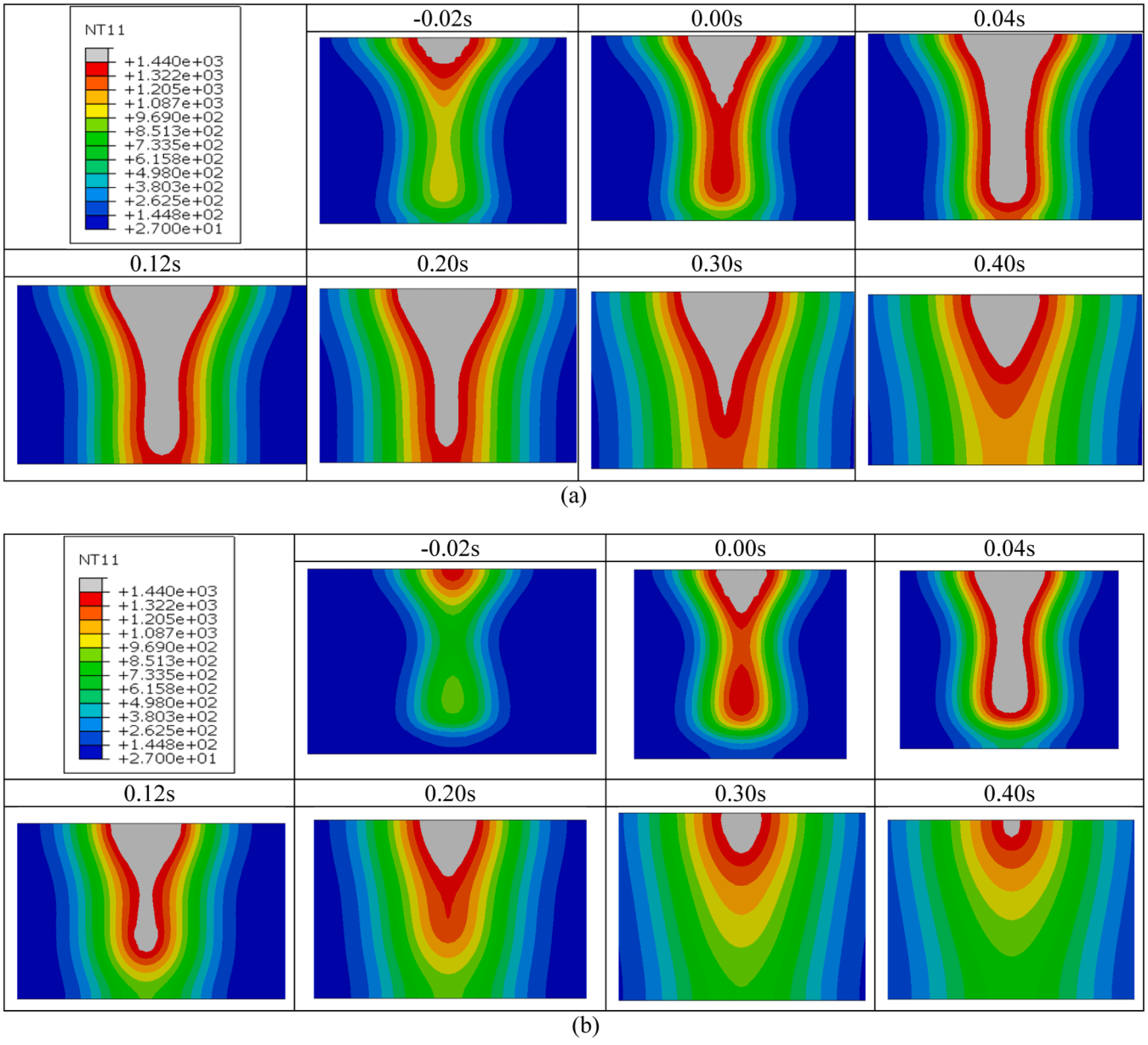

Fig. 14. Temperature distribution over time at welding speeds of (a) 1.0 and (b) 1.5 m/min.

Table 13
Dimensions of welding bead in Cases 1 and 2.

	Welding velocity (m/min)	Top bead width (mm)	Concave bead width (mm)	Concave bead depth (mm)	Penetration (mm)
Case 1	1.0	3.28	1.06	2.90	5.55
Case 2	1.5	2.69	0.83	2.29	4.50

for each case, is shown in Table 13. The cross-sectional shapes are shown in Figs. 15 and 16.

Optimal solutions were derived by minimizing the objective function from among candidate solutions that meet the constraints. The constraints ensure that the temperature along the bead line momentarily exceeds the melting point inside the bead and never outside the bead line during the welding process.

Table 14 shows the values of independent variables for each welding

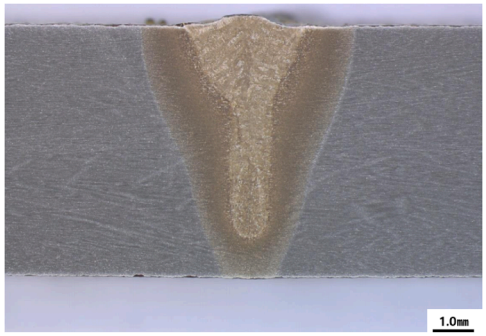

Fig. 15. Cross-sectional view of the specimen at the welding speed of 1.0 m/min (Case 1).

condition derived from the process described in Section 3. Table 15 shows the parameters of the welding heat source, which are calculated based on the values. The results of heat transfer analysis using the heat

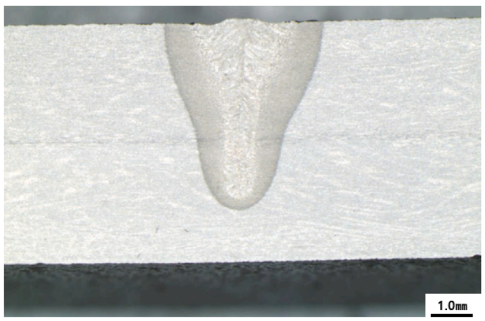

Fig. 16. Cross-sectional view of the specimen at the welding speed of 1.5 m/min (Case 2).

Table 14
Independent variable values in Cases 1 and 2.

Variables	Case 1	Case 2
η	0.833	0.818
R_{T1}	3.918	2.814
Heat depth $(y_{T1} - y_{T7})$	5.637	5.128
C_{RT1}	0.515	0.657
C_{RT2}	0.942	0.806
C_{RT3}	0.914	0.968
C_{RT4}	1.013	1.183
C_{RT5}	0.598	0.597
C_{RT6}	0.731	0.596
W_{HR1}	1.034	1.136

Table 15
Parameters of the welding heat source in Cases 1 and 2.

Variables	Case 1	Case 2
Efficiency (%)	83.3	81.8
R_{T1} (mm)	3.918	2.814
R_{T2} (mm)	2.019	1.849
R_{T3} (mm)	1.901	1.491
R_{T4} (mm)	1.738	1.444
R_{T5} (mm)	1.760	1.709
R_{T6} (mm)	1.933	1.875
R_{T7} (mm)	2.380	2.056
Heat depth (mm)	5.637	5.128
Heat ratio 1 (%)	34.0	30.1
Heat ratio 2 (%)	13.9	13.5
Heat ratio 3 (%)	12.0	10.4
Heat ratio 4 (%)	11.0	12.0
Heat ratio 5 (%)	12.3	15.5
Heat ratio 6 (%)	16.8	18.6

source model are described in Section 4.2. Table 15 shows that C_{RT4} exceeded one for all conditions, which means that the radius of each layer constituting the welding heat source decreases along the depth direction and then increases again at the middle point.

The proposed heat source model contains multiple parameters to be determined by the optimization process. To evaluate the stability and existence of the optimal solution, the optimization process was repeated multiple times with different initial values. The process was iterated four times for each scenario. The results are shown in Tables 16 and 17. For Case 1, it was found that the coefficient of variation (COV) in temperature distribution error was within 2.64%, while for Case 2, it was within 4.93%, which was acceptable.

4.2. Verification of the simplified model

The heat source models described above were derived through an optimization algorithm based on a simplified model. Therefore, it is essential to verify whether these models provide the same results as the results obtained under actual conditions. For verification, 3D models were configured based on actual experimental conditions, and each was analyzed. The shapes of both the original model and the simplified model are described in Section 3.

The temperature distribution was compared with that of the original model to verify the consistency of the simplified model. For comparison, the time taken for the boiling point area to reach its maximum after the heat source was checked, and the temperature distribution at that time was compared (Fig. 17). There was the delay of 0.1 seconds under the condition of 1.0 m/min and the delay of 0.06 seconds under the condition of 1.5 m/min. The temperature distribution at each condition was compared, as shown in Figs. 18 and 19. In Cases 1 and 2, temperature distributions mimic the experiment. To rigorously verify this, dimensions such as top bead width, penetration, concave bead width, and concave bead depth were compared with experimental results.

The primary difference between the 3D original model and the 2D simplified model lies in the consideration of heat transfer along the welding direction (X-direction). As shown in Eq. (18), heat flux (q'') in conduction heat transfer is determined by the gradient of the temperature distribution ($T(x, y, z)$) in each direction. Based on this principle, it was assumed that at the moment of maximum melting, heat transfer is more significant in the direction perpendicular to the welding process (Z-direction) than along the welding direction. This assumption was validated through simulations (Table 18). At the moment of maximum melting, the heat flux in the X-direction was found to be 13.6% of that in the Z-direction for Case 1 and 12.1% for Case 2.

$$\boldsymbol{q}'' = -k\nabla\left(\boldsymbol{i}\frac{\partial \boldsymbol{T}(x,y,z)}{\partial x} + \boldsymbol{j}\frac{\partial \boldsymbol{T}(x,y,z)}{\partial y} + \boldsymbol{k}\frac{\partial \boldsymbol{T}(x,y,z)}{\partial z}\right) \tag{18}$$

Individual results from the FEA simulations were compared with the corresponding experimental results for quantitative comparison. The comparisons are presented in Tables 19–22. As shown in Tables 21 and 22, the discrepancy between the original and simplified models was within 15%, and the deviation from the experimental results was within 11%. This error was attributed to the assumption of the 2D simplified model, which neglected heat transfer in the welding direction. The proposed simplified model demonstrated a high level of consistency

Table 16
Repeatability test results for Case 1.

Variables	Test 1	Test 2	Test 3	Test 4	Test 5	Average	Standard deviation	Coefficient of variation
η (%)	0.833	0.832	0.833	0.833	0.833	0.833	0.001	0.0005
R_{T1} (mm)	3.918	3.907	3.876	3.879	3.918	3.899	0.021	0.0047
Heat depth (mm)	5.637	5.618	5.647	5.638	5.637	5.635	0.011	0.0017
C_{RT1}	0.515	0.524	0.637	0.637	0.515	0.566	0.065	0.1032
C_{RT2}	0.942	0.943	0.915	0.915	0.942	0.931	0.015	0.0144
C_{RT3}	0.914	0.911	0.844	0.844	0.914	0.885	0.038	0.0382
C_{RT4}	1.013	1.012	1.049	1.050	1.013	1.027	0.020	0.0176
C_{RT5}	0.598	0.598	0.501	0.501	0.598	0.559	0.053	0.0850
C_{RT6}	0.731	0.730	0.818	0.818	0.731	0.766	0.048	0.0559
W_{HR1}	1.034	1.034	1.048	1.046	1.034	1.039	0.007	0.0062
Temperature distribution error (°C)	34.4	32.1	33.6	34.0	34.6	33.8	1.0	0.0264

Table 17
Repeatability test results for Case 2.

Variables	Test 1	Test 2	Test 3	Test 4	Test 5	Average	Standard deviation	Coefficient of variation
η (%)	0.818	0.819	0.815	0.812	0.815	0.816	0.003	0.0030
$R_{T1\ (mm)}$	2.814	2.683	2.674	2.715	2.682	2.714	0.058	0.0192
Heat depth (mm)	5.128	5.161	5.199	5.394	5.201	5.217	0.103	0.0178
C_{RT1}	0.657	0.654	0.662	0.694	0.667	0.667	0.016	0.0214
C_{RT2}	0.806	0.837	0.840	0.823	0.841	0.829	0.015	0.0161
C_{RT3}	0.968	0.978	0.999	0.924	0.999	0.974	0.031	0.0283
C_{RT4}	1.183	1.187	1.171	1.170	1.136	1.169	0.020	0.0154
C_{RT5}	0.597	0.535	0.509	0.543	0.533	0.543	0.032	0.0536
C_{RT6}	0.596	0.683	0.544	0.593	0.558	0.595	0.054	0.0814
W_{HR1}	1.136	1.173	1.178	1.140	1.178	1.161	0.021	0.0163
Temperature distribution error (°C)	12.2	11.2	12.6	12.5	13.0	12.3	0.7	0.0493

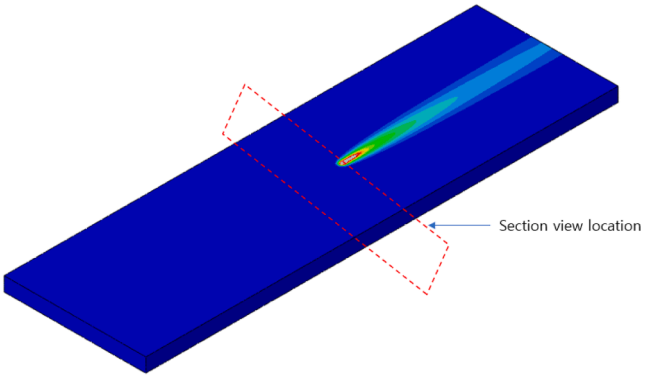

Fig. 17. The location of section views to check the temperature distribution of the 3D model.

while significantly reducing simulation time from over 480 hours to just 0.25 hours as presented in Table 12. This improvement ensures its feasibility for real-time application in industrial settings. Nonetheless, further research is needed to enhance the model's accuracy by addressing its current limitations.

4.3. Discussion

Two cases were analyzed in this study. It was found that C_{RT4} exceeded one in all cases. That means the heat sources are similar to the shape of a dual truncated cone combination, from among the welding heat source shapes proposed before. For a more detailed comparison, the top radius (R_{T1}), mid radius (R_{T4}), bottom radius (R_{T7}), and heat depth were selected as representative parameters constituting the welding heat source. The sizes were compared according to the welding speed, as shown in Figs. 20 and 21.

It was found that the radius of a welding heat source decreased linearly as shown in Fig. 20. In particular, it was confirmed that the decrease rate in the size of the top radius was larger than that of the mid radius and the bottom radius, which means that the shape of a heat

Table 18
Maximum heat flux in each direction at the moment of maximum melting (W/mm).

	Welding direction (X-axis)	Welding orthogonal direction (Z-axis)	Ratio (%)
Case 1	2.43×10^4	3.30×10^3	13.6
Case 2	2.15×10^4	2.62×10^3	12.1

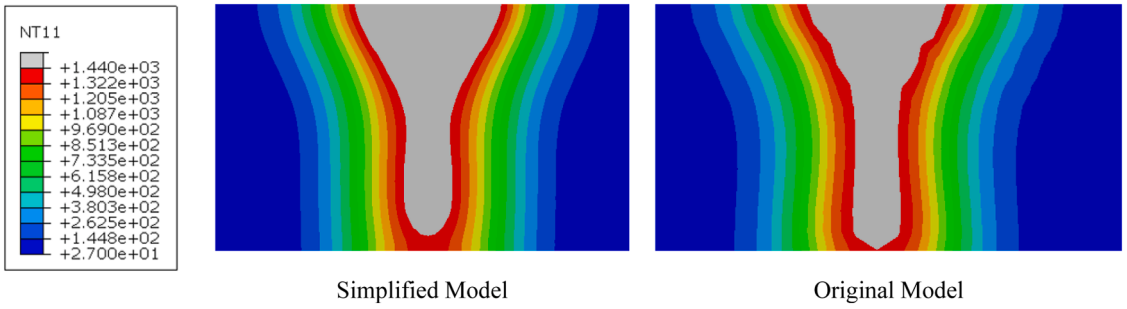

Fig. 18. Comparison of the temperature distribution at 1.0 m/min (Case 1) of the simplified model and the original model.

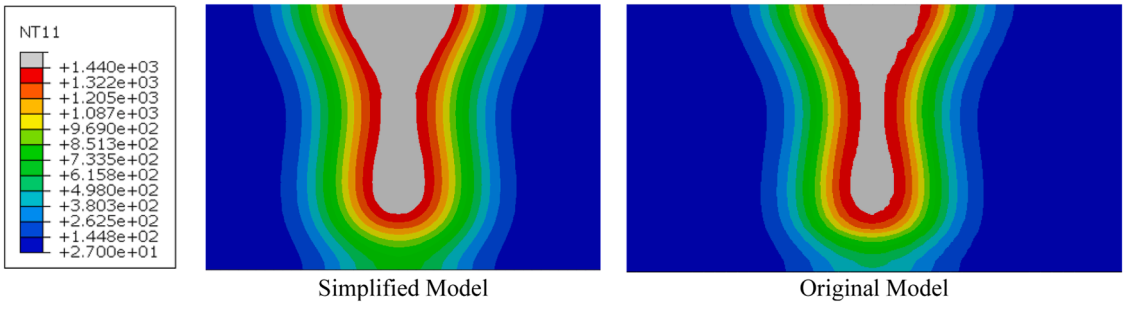

Fig. 19. Comparison of the temperature distribution at 1.5 m/min (Case 2) of the simplified model and the original model.

Table 19
Dimension of the welding bead for the 1.0 m/min speed.

	Top bead width (mm)	Concave bead width (mm)	Concave bead depth (mm)	Penetration (mm)
Experiment	3.28	1.06	2.90	5.55
Simplified model	3.58	1.20	2.71	5.58
Original model	3.30	1.00	3.00	5.90

Table 20
Dimension of the welding bead for the 1.5 m/min speed.

	Top bead width (mm)	Concave bead width (mm)	Concave bead depth (mm)	Penetration (mm)
Experiment	2.69	0.84	2.29	4.51
Simplified model	2.58	0.78	2.23	4.82
Original model	2.30	0.75	2.00	4.73

Table 21
Accuracy of simulation models for the 1.0 m/min speed.

	Top bead width (%)	Concave bead width (%)	Concave bead depth (%)	Penetration (%)
Simplified model to experiment	2.74	1.42	0.52	0.54
Original model to experiment	0.61	5.66	3.45	6.31
Simplified model to original model	2.08	6.98	2.92	5.73

Table 22
Accuracy of simulation models for the 1.5 m/min speed.

	Top bead width (%)	Concave bead width (%)	Concave bead depth (%)	Penetration (%)
Simplified model to experiment	4.02	7.54	2.90	7.16
Original model to experiment	14.54	10.53	12.82	5.00
Simplified model to original model	10.96	3.23	10.21	2.01

source becomes more like a dual truncated cone combination shape as the welding speed gets faster. For a quantitative evaluation, the ratio between the radii under the conditions was checked; as shown in Table 23, it was found that the sizes of the top radius and bottom radius decreased as the welding speed increased. Also, the depth of the heat source decreased as the speed increased, as shown in Fig. 21.

The analysis confirmed that the level 2 model struggles to replicate heat sources with mid-point inflections accurately as demonstrated in Table 24. Furthermore, it was observed that the shape of a lower heat source can differ significantly from that of the existing heat sources. The level 3 model proposed in this study represents an advanced approach as a representative heat source model, incorporating considerations from existing heat source models proposed in the prior research (Fig. 22).

The multi-layer-based geometry enables the precise construction of heat source models tailored to diverse shapes and allows for the customization of models to fit specific conditions. The findings of this study suggest that the dual truncated cone shape with a curved bevel is particularly suitable for these scenarios. This represents a more advanced form than the existing dual truncated cone shape, as evidenced by a 2.8 times reduction in the temperature error. Without the proposed model, accurately predicting the weld zone becomes challenging, especially when different base materials and shapes are considered.

A comparative analysis was performed to evaluate the proposed heat source model against existing models, including the cone [32], truncated cone [33–35], truncated cone with a curved bevel [36,37], and combined shapes [38–41]. The FEA results using the proposed model most accurately represented the temperature distribution compared to experimental data (Fig. 23). The melting zone, shown in gray, is a key factor in assessing model accuracy. Compared to existing models, the proposed model demonstrated the highest accuracy. Table 25 presents a quantitative comparison of temperature agreement with the experiment. The proposed model showed minimal errors in both cases, while the best existing model, the double truncated cone, exhibited nearly twice these errors. These findings underscore the superior accuracy of the proposed model.

Finding the optimal number of layers is essential. While more layers allow for a more precise representation of the heat source shape, they also increase the number of variables to optimize, leading to higher computational costs and a greater risk of local optima. In contrast, fewer layers reduce accuracy in capturing the heat source shape. To determine the optimal number of layers, five cases were analyzed, ranging from two to ten layers. Even numbers were chosen to align with existing heat sources, which exhibit inflection points at mid-height, and to ensure precise configuration. As shown in Tables 26–28, the comparison identified the six-layer model as the most effective, supporting its selection for this study.

This study employed MIGA to achieve global optimization effectively. This method improves upon conventional genetic algorithms by dividing the initial population into several islands that evolve independently, with periodic migrations between them. It is particularly effective for deriving global nondominated solutions [55,56]. Given its suitability for small-scale problems [66], MIGA was selected. Other global optimization methods, such as the downhill simplex method [67], evolutionary optimization [68], and particle swarm optimization [69], were compared. Consequently, MIGA was found to be the most effective, as shown in Table 29.

Major shipbuilders are increasingly adopting them for manufacturing cryogenic fuel storage containers as the cost of laser welding systems decreases [70]. Predicting weld distortion during fiber laser welding for Type C tanks and membrane-type tanks is a paramount task. In response to this demand, this study presents a laser welding heat source for cryogenic steels, including 9% nickel steel. The proposed multi-layered heat source model has the potential to be implemented in most weldable materials such as stainless steel 304L and 316L, and 36% nickel steel (invar).

This study enables the derivation of welding heat sources tailored to field requirements and facilitates precise welding simulations. Additionally, it allows for more accurate predictions of welding deformation and residual stress at the simulation stage, contributing to the determination of optimal welding conditions. Ultimately, it is expected to support welding automation through advanced simulations. Furthermore, its applicability can be extended beyond fiber laser welding to high-heat input welding such as electron beam welding. The technology can be used not only in the welding field but also in laser-based surface treatment and machining applications [71,72].

5. Conclusions and future works

This study proposed a novel multi-layered heat source model for laser welding FEA simulations of cryogenic materials. The proposed multi-layered heat source model was never reported in the literature, although implementing a precise heat source model to FEA significantly affects the prediction of weld distortion and residual stress. The FEA

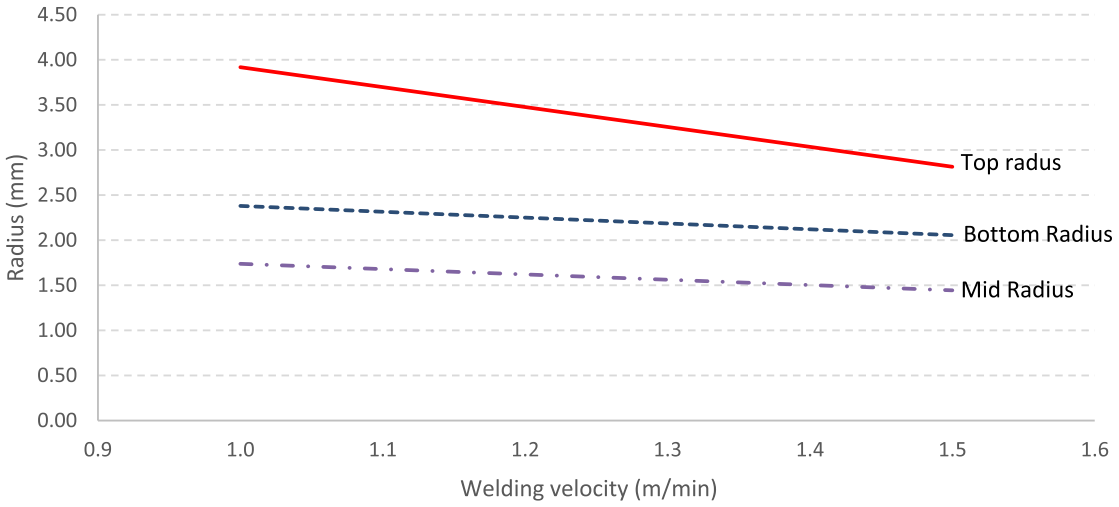

Fig. 20. Correlation of the heat source radius according to the welding speed.

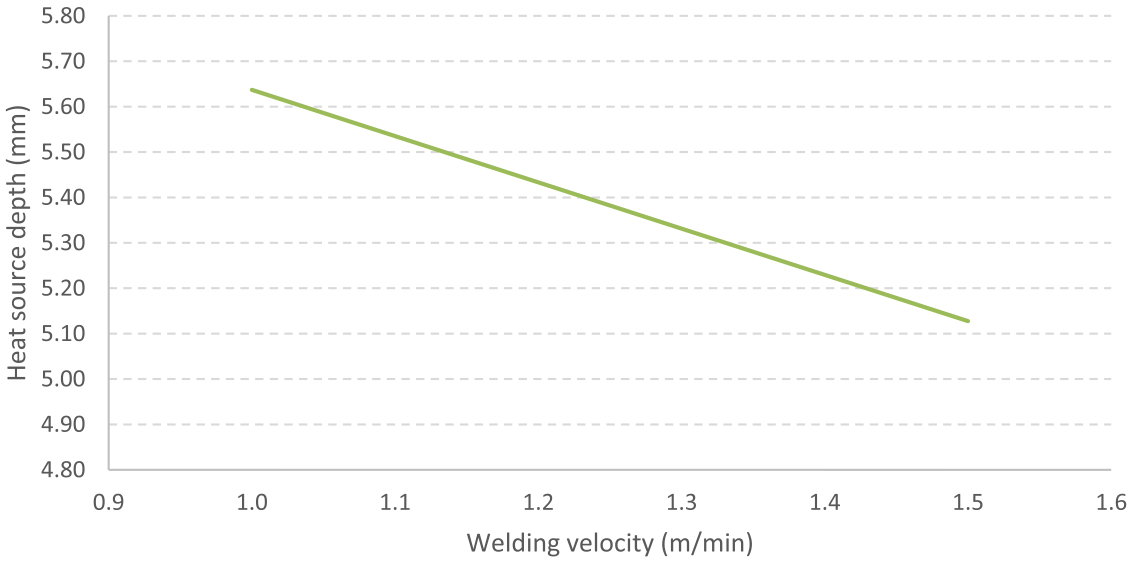

Fig. 21. Correlation of the heat source height according to the welding speed.

Table 23
The ratio of radius in Cases 1 and 2.

	Case 1	Case 2
Top radius/Mid radius	2.25	1.95
Bottom radius/Mid radius	1.37	1.42
Top radius/Bottom radius	1.65	1.37

Table 24
Parameters of the welding heat source with the level 2 model.

Variables	Case 1	Case 2
Efficiency (%)	81.9	80.7
R_{T1} (mm)	3.650	2.708
R_{T2} (mm)	2.035	2.233
R_{T3} (mm)	1.922	1.292
R_{T4} (mm)	1.917	1.276
R_{T5} (mm)	2.344	1.294
R_{T6} (mm)	0.913	3.171
Heat depth (mm)	7.170	5.571
Heat ratio 1 (%)	36.7	34.6
Heat ratio 2 (%)	16.5	17.7
Heat ratio 3 (%)	15.6	9.2
Heat ratio 4 (%)	19.2	9.2
Heat ratio 5 (%)	11.9	29.4

results using the proposed model with optimized parameters outperformed existing ones subjected to multiple operational conditions. The experimental results showed that the proposed multi-layered heat source model had only a 1.6% error on average, whereas the state-of-the-art model, the double truncated cone model, showed a 4.5% error.

The prediction of the residual stress and thermal distortion in fiber laser welding is not an easy task, especially when the heat source models have many unknown parameters. To address this challenge, in this study, a systematic approach by solving inverse problems was proposed to estimate the parameters of the proposed heat source model. The proposed systematic approach consists of (1) obtaining melting zone boundary images from experiments, (2) defining model parameters, (3) predicting the melting zone boundary from the FEA simulations, (4) estimating the heat source model parameters by minimizing the agreement between experimental and FEA responses, (5) predicting the melting zone boundary of welding specimen in the field. This systematic approach will help enhance the quality of welds in fiber laser welding.

The simplified FEA model proposed in this study can accelerate the

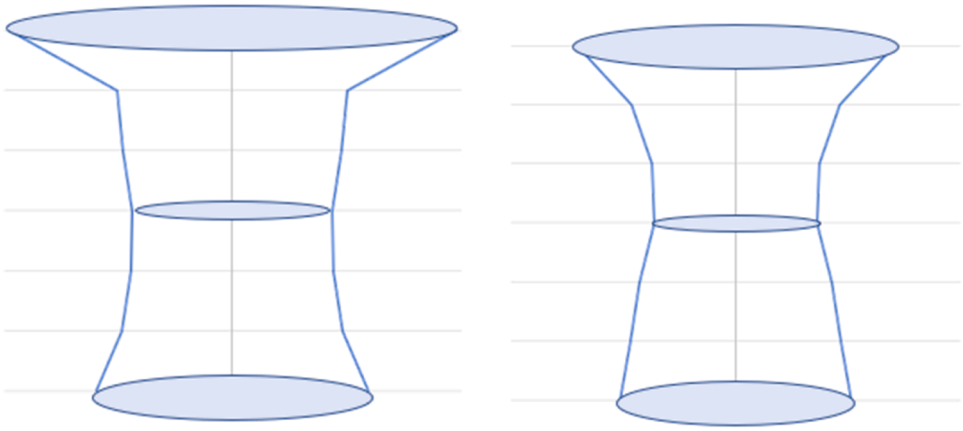

Fig. 22. Shape of the level 3 heat source model (a) Case 1 and (b) Case 2.

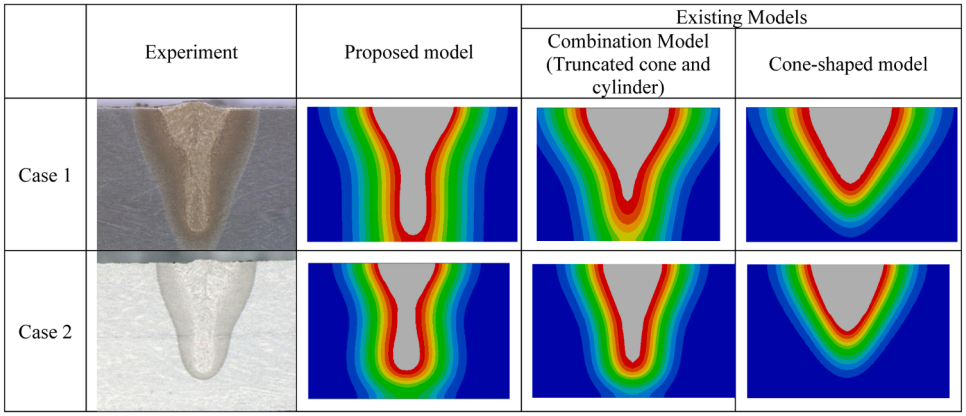

Fig. 23. Comparison of temperature distributions from experiments with various heat source model predictions.

Table 25
Temperature distribution errors at the melting zone boundary.

	Proposed model	Existing model					
	Multi-layered shape	Cone	Truncated cone	Truncated cone with curved bevel	Truncated cone and cylinder	Double truncated cone	Goldak Model
Case 1 (°C)	34.4	495.7	94.8	150.4	235.6	96.2	470.0
Case 2 (°C)	12.2	668.3	114.1	105.3	165.8	33.7	632.0
Average error (°C)	23.3 (1.6%)	582.0 (40.1%)	104.5 (7.2%)	127.9 (8.8%)	200.7 (13.8%)	65.0 (4.5%)	551.0 (38.0%)

Table 26
Temperature distribution errors at the melting zone boundary by the number of layers (Case 1).

	Six layers (Proposed model)	Two layers	Four layers	Eight layers	Ten layers
Average error (°C)	34.4 (2.4%)	93.2 (6.6%)	38.2 (2.6%)	49.4 (3.4%)	63.0 (4.3%)

FEA procedure. Finding optimal model parameters can be achieved by multiple iterations in the optimization process, which requires a significant number of computational resources. The effectiveness of the simplified FEA model was demonstrated in solving the inverse problem. The experimental results showed that the computational cost was reduced by 1/2000 while maintaining the prediction accuracy at the melting zone boundary.

This study conducted theoretical and practical analysis on the multi-layered heat source model for fiber laser welding of cryogenic nickel

Table 27
Dimension of the welding bead by the number of layers (Case 1).

	Experiment	Six layers (Proposed model)	Two layers	Four layers	Eight layers	Ten layers
Top bead width (mm)	3.28	3.58	3.75	3.12	2.97	2.85
Concave bead width (mm)	1.06	1.20	0.81	0.81	1.40	1.40
Concave bead depth (mm)	2.90	2.71	3.10	2.89	2.91	3.10
Penetration (mm)	5.55	5.58	5.94	5.50	5.04	5.15

Table 28
The error rate of the welding bead by the number of layers (Case 1).

	Six layers (Proposed model)	Two layers	Four layers	Eight layers	Ten layers
Top bead width (%)	9.15	14.33	4.88	9.45	13.11
Concave bead width (%)	13.21	23.58	23.58	32.08	32.08
Concave bead depth (%)	6.55	6.90	0.34	0.34	6.90
Penetration (%)	0.54	7.03	0.90	9.19	7.21

Table 29
Temperature distribution errors at the melting zone boundary by optimization method (Case 1).

	MIGA (Proposed model)	Downhill simplex	Particle swarm	Evolutionary
Average error (°C)	34.4 (2.4%)	98.5 (6.8%)	43.5 (3.0%)	40.3 (2.8%)

steel. Nonetheless, a couple of limitations in the current study were identified for future work.

First, the computational cost required to analyze full simulation models is still prohibitive for on-site applications, particularly in the prediction of weld distortion and residual stress during fiber laser welding. To accelerate the simulation, reduced order models for CFD can be considered to capture the phase transformation and dynamics of the molten pool during welding.

Second, the consistency of temperature profiles, including heating and cooling rates, will be considered to enhance the accuracy of the heat source model. The temperature profile can serve as an indicator for assessing how well the model replicates experimental conditions. Incorporating that as an objective function is expected to yield a heat source model that more accurately reflects.

Third, solving optimization-based inverse problems across various welding conditions presents a challenge, primarily due to the lack of timeliness for real-time on-site applications. Deep learning-based surrogate models can be considered to address this issue. Further research will also explore the application of this technology to other commercial software platforms used in the field, including Sysweld, Ansys, and Simufact, in addition to Abaqus.

Fourth, this study applied a 2D-based simplified model that reduced simulation time by a factor of 1/2000, enhancing real-time applicability in industrial settings. However, this approach has limitations in perfectly replicating actual experimental results. To address this issue, model accuracy will be improved by incorporating interpolation methods that account for heat flux magnitude in each direction. Since this is a nonlinear heat transfer problem, extensive case studies will be conducted to analyze the relationship of heat flux in different directions, and an interpolation method will be applied based on these values.

Fifth, this study will develop a database of heat source shapes corresponding to various welding conditions and materials. This database aims to enable real-time welding simulations in practical applications. For field implementation, accuracy and reproducibility must be ensured beginning from the experimental stage of cross-section extraction. To achieve this, cross-sections validated through multiple experiments will be used to enhance the accuracy of the welding heat source.

Finally, to accommodate potential variations encountered in practical applications, heat source models will be developed within a range that allows for non-uniform welding speeds and power at key points of variation. Interpolation will be used to adjust heat source parameters according to specific scenarios, enhancing the model's practical applicability in real-world conditions.

Declaration of competing interest

The authors declare that they have no known competing financial interests or personal relationships that could have appeared to influence the work reported in this paper.

Acknowledgment

This research was supported by National R&D Program through the National Research Foundation of Korea (NRF) funded by Ministry of Science and ICT (2021M3H4A3A02098099), and also this work was supported by the InnoCORE program of the Ministry of Science and ICT (N10250154).

References

[1] Y. Cao, Q. Jia, S. Wang, Y. Jiang, Y. Bai, J. Ocean Eng. Sci. 7 (2022) 75–83, https://doi.org/10.1016/j.joes.2021.06.001.
[2] N. Abdussamie, M. Daboos, I. Elferjani, C. Shuhong, A. Alaktiwi, J. Ocean Eng. Sci. 3 (2018) 56–66, https://doi.org/10.1016/j.joes.2017.12.002.
[3] G. Marroni, V.Casson Moreno, F. Ovidi, T. Chiavistelli, G. Landucci, Ocean Eng. 273 (2023) 114019, https://doi.org/10.1016/j.oceaneng.2023.114019.
[4] D.-H. Park, M.-S. Yi, J.-M. Lee, J. Weld. Join. 40 (2022) 118–132, https://doi.org/10.5781/jwj.2022.40.2.3.
[5] C. Ye, Y. Lin, Ocean Eng. 262 (2022) 112233, https://doi.org/10.1016/j.oceaneng.2022.112233.
[6] T.-U. Park, D.-H. Jung, J.-H. Park, J.-H. Kim, I.-W. Han, J. Weld. Join. 40 (2022) 33–39, https://doi.org/10.5781/jwj.2022.40.1.4.
[7] T.-J. Yun, W.-B. Oh, B.-R. Lee, C.-W. Lee, H.-H. Na, J.-S. Choi, I.-S. Kim, J. Weld. Join. 38 (2020) 485–492, https://doi.org/10.5781/JWJ.2020.38.5.8.
[8] B.E. Kim, J.-Y. Park, J.S. Lee, M.-H. Kim, J. Weld. Join. 37 (2019) 555–563, https://doi.org/10.5781/JWJ.2019.37.6.4.
[9] H.T. Serindağ, C. Tardu, İ.Ö. Kirçiçek, G. Çam, CIRP J. Manuf. Sci. Technol. 37 (2022) 1–10, https://doi.org/10.1016/j.cirpj.2021.12.006.
[10] A. Veríssimo Passos, F.W.C. Farias, V.H.P. Moraes e Oliveira, M.C.G. Rios, J. C. Payão, Constr. Build. Mater. 282 (2021) 122573, https://doi.org/10.1016/j.conbuildmat.2021.122573.
[11] T.-U. Park, Y.-C. Jeong, H.-D. Im, C. Choi, W. Kil, J. Weld. Join. 40 (2022) 367–376, https://doi.org/10.5781/jwj.2022.40.5.1.
[12] Y. Chen, B. Chen, Y. Yao, C. Tan, J. Feng, NDT E Int 108 (2019) 102176, https://doi.org/10.1016/j.ndteint.2019.102176.
[13] D. Sun, K. Dilger, J. Adv. Join. Process. 8 (2023) 100157, https://doi.org/10.1016/j.jajp.2023.100157.
[14] S. Kang, J. Shin, Opt. Laser Technol. 158 (2023) 108805, https://doi.org/10.1016/j.optlastec.2022.108805.
[15] T. Sibillano, D. Rizzi, A. Ancona, S. Saludes-Rodil, J.Rodríguez Nieto, H. Chmelíčková, H. Šebestová, J. Mater. Process. Technol. 212 (2012) 910–916, https://doi.org/10.1016/j.jmatprotec.2011.11.016.
[16] N.S. Hosseini Motlagh, P. Parvin, M. Jandaghi, M.J. Torkamany, Opt. Laser Technol. 54 (2013) 191–198, https://doi.org/10.1016/j.optlastec.2013.04.027.
[17] M.M.A. Kharter, Int. J. Mod. Phys. B 37 (2023) 2350083, https://doi.org/10.1142/S0217979223500832.
[18] M.M.A. Khater, Chaos Solitons Fractals 169 (2023) 113232, https://doi.org/10.1016/j.chaos.2023.113232.
[19] M.M.A. Khater, S.H. Alfalqi, J.F. Alzaidi, R.A.M. Attia, Results Phys 46 (2023) 106312, https://doi.org/10.1016/j.rinp.2023.106312.
[20] M.M.A. Khater, Chaos Solitons Fractals 167 (2023) 113098, https://doi.org/10.1016/j.chaos.2022.113098.
[21] Y. Feng, X. Gao, Y. Zhang, Int. J. Adv. Manuf. Technol. 112 (2021) 2301–2312, https://doi.org/10.1007/s00170-020-06489-y.
[22] Y. Rong, L. Wang, R. Wu, J. Xu, Int. J. Therm. Sci. 171 (2022) 107257, https://doi.org/10.1016/j.ijthermalsci.2021.107257.
[23] A. Evdokimov, N. Doynov, R. Ossenbrink, A. Obrosov, S. Weiß, V. Michailov, Int. J. Mech. Sci. 190 (2021) 106019, https://doi.org/10.1016/j.ijmecsci.2020.106019.
[24] Y. Rong, T. Lei, J. Xu, Y. Huang, C. Wang, Int. J. Mech. Sci. 146–147 (2018) 180–190, https://doi.org/10.1016/j.ijmecsci.2018.07.046.
[25] N. Azari-Dodaran, H. Ahmadi, J. Ocean Eng. Sci. 4 (2019) 352–372, https://doi.org/10.1016/j.joes.2019.05.009.
[26] N. Rathinam, B. Parbu, D. Anbazhaghan, J. Ocean Eng. Sci. 6 (2021) 360–366, https://doi.org/10.1016/j.joes.2021.03.002.
[27] S.B. Pranesh, D. Kumar, V. Subramanian, D. Sathianarayanan, G.A. Ramadass, J. Ocean Eng. Sci. 2 (2017) 293–300, https://doi.org/10.1016/j.joes.2017.11.001.
[28] Q.-H. Zhou, H.-X. Xue, K.-Y. Hu, H.-R. Liu, W.-L. Tu, J. Ocean Eng. Sci. (2025), https://doi.org/10.1016/j.joes.2025.04.001. In press.
[29] J. Yi, J. Lin, Z. Chen, T. Chen, J. Ocean Eng. Sci. 6 (2021) 410–416, https://doi.org/10.1016/j.joes.2021.06.002.
[30] D. Saini, D. Karmakar, S. Ray-Chaudhuri, J. Ocean Eng. Sci. 1 (2016) 186–202, https://doi.org/10.1016/j.joes.2016.06.006.
[31] Z. Barsoum, Guidelines for Fatigue and Static Analysis of Welded and Un-Welded Steel Structures, KTH Royal Institute of Technology, 2020, pp. 31–38.

[32] J. Kim, B.S. Jang, Y.T. Kim, K.S. Chun, Int. J. Nav. Archit. Ocean Eng. 5 (2013) 348–363, https://doi.org/10.2478/IJNAOE-2013-0138.
[33] F. Farrokhi, B. Endelt, M. Kristiansen, Opt. Laser Technol. 111 (2019) 671–686, https://doi.org/10.1016/j.optlastec.2018.08.059.
[34] S. He, S. Chen, Y. Zhao, N. Qi, X. Zhan, J. Manuf. Process. 63 (2021) 121–129, https://doi.org/10.1016/j.jmapro.2020.04.043.
[35] Z. Lei, J. Zou, D. Wang, Z. Guo, R. Bai, H. Jiang, C. Yan, Opt. Laser Technol. 129 (2020) 106289, https://doi.org/10.1016/j.optlastec.2020.106289.
[36] G.X. Xu, C.S. Wu, G.L. Qin, X.Y. Wang, S.Y. Lin, Int. J. Adv. Manuf. Technol. 57 (2011) 245–255, https://doi.org/10.1007/s00170-011-3274-x.
[37] A. Evdokimov, K. Springer, N. Doynov, R. Ossenbrink, V. Michailov, Int. J. Adv. Manuf. Technol. 93 (2017) 709–716, https://doi.org/10.1007/s00170-017-0569-6.
[38] T. Kik, Mater 13 (2020) 2653, https://doi.org/10.3390/ma13112653.
[39] J.R. Chukkan, M. Vasudevan, S. Muthukumaran, R.Ravi Kumar, N. Chandrasekhar, J. Mater. Process. Technol. 219 (2015) 48–59, https://doi.org/10.1016/j.jmatprotec.2014.12.008.
[40] V. Busto, D. Coviello, A. Lombardi, M. Vito, D. Sorgente, Int. J. Adv. Manuf. Technol. 119 (2022) 137–148, https://doi.org/10.1007/s00170-021-08217-6.
[41] A.K. Unni, M. Vasudevan, Today Proc 45 (2021) 4465–4471, https://doi.org/10.1016/j.matpr.2020.12.842.
[42] F. Giudice, S. Missori, A. Sili, Int. J. Adv. Manuf. Technol. 112 (2021) 1339–1358, https://doi.org/10.1007/s00170-020-06479-0.
[43] F. Giudice, A. Sili, Metals 13 (2023) 2020, https://doi.org/10.3390/met13122020.
[44] F. Giudice, A. Sili, Int. J. Adv. Manuf. Technol. 123 (2022) 2793–2808, https://doi.org/10.1007/s00170-022-10247-7.
[45] E.J.G. Nascimento, E. dos Santos Magalhães, L. dos Santos Paes, Int. J. Adv. Manuf. Technol. 126 (2023) 2917–2957, https://doi.org/10.1007/s00170-023-11253-z.
[46] J. Goldak, A. Chakravarti, M. Bibby, Metall. Trans. B 15 (1984) 299–305, https://doi.org/10.1007/BF02667333.
[47] A.K. Mondal, B. Kumar, S. Bag, Y. Nirsanametla, P. Biswas, Int. J. Therm. Sci. 166 (2021) 107005, https://doi.org/10.1016/j.ijthermalsci.2021.107005.
[48] C. Pyo, J. Kim, D.S. Kim, Processes 9 (2021) 2188, https://doi.org/10.3390/pr9122188.
[49] C. Pyo, J. Kim, Y. Kim, M. Kim, Mar. Struct. 86 (2022) 103260, https://doi.org/10.1016/j.marstruc.2022.103260.
[50] C. Pyo, J. Korean Soc. Mech. Technol. 24 (2022) 549–554.
[51] C. Pyo, S.-M. Jeong, J. Kim, M. Park, J. Shin, Y. Kim, J. Son, J.-M. Kim, M.-H. Kim, J. Mar. Sci. Eng. 10 (2022) 1810, https://doi.org/10.3390/jmse10121810.
[52] V. Ciancio, Int. J. Math. Comput. Eng. 2 (2024) 1–14, https://doi.org/10.2478/ijmce-2024-0011.
[53] M. Park, J. Kim, C. Pyo, Metals 12 (2022) 1195, https://doi.org/10.3390/met12071195.
[54] S. Katoch, S.S. Chauhan, V. Kumar, Multimed. Tools Appl. 80 (2021) 8091–8126, https://doi.org/10.1007/s11042-020-10139-6.
[55] T. Shi, M. Pang, Y. Wang, Y. Zhang, Eng. Fract. Mech. 300 (2024) 110005, https://doi.org/10.1016/j.engfracmech.2024.110005.
[56] W. Zhang, H. Qi, Z. Yu, M. He, Y. Ren, Y. Li, Sol. Energy 224 (2021) 947–955, https://doi.org/10.1016/j.solener.2021.06.059.
[57] K. Lee, W. Kim, J. Lee, C. Park, J. Yang, T. Kim, J. Park, J. Mech. Sci. Technol. 23 (2009) 2948–2955.
[58] M. Bramson, Infrared Radiation, a Handbook for Applications, Springer US, 2013, p. 535.
[59] P. Pankaj, P.S. Sawarkar, A. Tiwari, P. Biswas, S. Pal, Today Proc 41 (2021) 902–907, https://doi.org/10.1016/j.matpr.2020.09.484.
[60] E. Erişir, İ.İ. Ayhan, C. Güney, E. Alan, N.B. Dürger, S. Ün, J. Mater. Eng. Perform. 30 (2021) 3458–3467, https://doi.org/10.1007/s11665-021-05689-1.
[61] G. Casalino, M. Mortello, N. Contuzzi, F.M.C. Minutolo, Procedia CIRP 33 (2015) 434–439, https://doi.org/10.1016/j.procir.2015.06.099.
[62] M. Imran, D. Shi, L. Tong, H.M. Waqas, Ocean Eng 190 (2019) 106443, https://doi.org/10.1016/j.oceaneng.2019.106443.
[63] Q. Yang, G. Guan, Ocean Eng 208 (2020) 107429, https://doi.org/10.1016/j.oceaneng.2020.107429.
[64] F. Erdogan, Int. J. Math. Comput. Eng. 2 (2024) 85–96, https://doi.org/10.2478/ijmce-2024-0007.
[65] O. Ilhan, G. Sahin, Int. J. Math. Comput. Eng. 2 (2024) 125–140, https://doi.org/10.2478/ijmce-2024-0010.
[66] C. Kim, H. Oh, B. Jung, S. Moon, Struct. Health Monit. 21 (2022) 2354–2369, https://doi.org/10.1177/14759217211056557.
[67] P. Raska, Z. Ulrych, Procedia Eng 100 (2015) 807–815, https://doi.org/10.1016/j.proeng.2015.01.435.
[68] Y. Jin, H. Wang, T. Chugh, D. Guo, K. Miettinen, IEEE Trans. Evol. Comput. 23 (2019) 442–458, https://doi.org/10.1109/TEVC.2018.2869001.
[69] S. Fan, Y. Liang, E. Zahara, Comput. Ind. Eng. 50 (2006) 401–425, https://doi.org/10.1016/j.cie.2005.01.022.
[70] Samsung Heavy develops high-speed welding robot for LNG carriers, LNGPrime, 2023. Sep. 25, https://lngprime.com/research-and-development/samsung-heavy-develops-high-speed-welding-robot-for-lng-carriers/92690 (accessed 3 April 2024).
[71] Y. Zhou, Q. Zhang, X. Li, Y. Wang, Y. Guan, J. Mater. Res. Technol. 33 (2024) 6084–6089, https://doi.org/10.1016/j.jmrt.2024.10.224.
[72] M. Xin, Z. Fan, L. Lu, Y. Guan, Weld. World 68 (2024) 3033–3050, https://doi.org/10.1007/s40194-024-01704-w.